

Isostasy with Love: II Airy compensation arising from viscoelastic relaxation

Mikael Beuthe

Royal Observatory of Belgium, Brussels, Belgium

mikael.beuthe@observatory.be

Abstract

In modern geodynamics, isostasy can be viewed either as the static equilibrium of the crust that minimizes deviatoric stresses, or as a dynamic process resulting from the viscous relaxation of the non-hydrostatic crustal shape. Paper I gave a general formulation of Airy isostasy as an elastic loading problem solved with Love numbers, and applied it to the case of minimum stress isostasy. In this sequel, the same framework is used to study Airy isostasy as the long-time evolution of a viscoelastic shell submitted to surface and internal loads. Isostatic ratios are defined in terms of time-dependent deviatoric Love numbers. Dynamic isostasy depends on the loading history, two examples of which are the constant load applied on the surface in the far past and the constant shape maintained by addition or removal of material at the compensation depth. The former model results in a shape decreasing exponentially with time and has no elastic analog, whereas the latter (stationary) model is equivalent to a form of elastic isostasy. Viscoelastic and viscous approaches are completely equivalent. If both load and shape vary slowly with time, isostatic ratios look like those of the stationary model. Isostatic models thus belong to two independent groups: the elastic/stationary approaches and the time-dependent approaches. If the shell is homogeneous, all models predict a similar compensation of large-scale gravity perturbations. If the shell rheology depends on depth, stationary models predict more compensation at long wavelengths, whereas time-dependent models result in negligible compensation. Mathematica and Fortran codes are available for computing the isostatic ratios of an incompressible body with three homogeneous layers.

Contents

1	Introduction	4
2	Isostatic ratios in terms of deviatoric Love numbers	9
2.1	Loading the shell	9
2.2	Isostatic ratios	13
3	Viscoelastic isostasy	14
3.1	Time-dependent Love numbers	14
3.2	Correspondence principle	15
3.3	Constant load	17
3.4	Constant shape	20
3.5	Variable load and shape	22
4	Viscous isostasy	22
4.1	Slow viscous flow	22
4.2	Stokes-Rayleigh analogy	23
4.3	Propagator matrix approach	23
4.4	Constant load	24
4.5	Constant shape	25
5	Application to Enceladus and Europa	27
5.1	Interior models and computational methods	27
5.2	Uniform viscosity	28
5.3	Depth-dependent rheology	29
6	Conclusions	31
	Appendix A Elastic isostasy	34
	Appendix B Constant loading of a homogeneous shell	36
B.1	Viscoelastic Love numbers	36
B.2	Poles and decay times	37
B.3	Residues	38
B.4	Thin shell limit	38
B.5	Shape ratio at high harmonic degree	39
	Appendix C Slow viscous flow	40
C.1	Differential equations	40
C.2	Fundamental matrices	41
C.3	Propagator matrices	43
C.4	Boundary conditions	44
C.5	Reduced propagation system	45

List of Figures

1	Viscoelastic relaxation of a two-layer spherical body	6
2	Relations between elastic, viscoelastic, and viscous isostatic models	8
3	Loading of a viscoelastic shell	10
4	Radial displacement of shell boundaries under a constant degree-two load	15
5	Viscoelastic/viscous isostasy with constant load: benchmarking	26
6	Elastic/viscoelastic/viscous isostasy with constant shape: benchmarking	27
7	Viscoelastic isostasy for a homogeneous shell: application to Enceladus and Europa .	30
8	Asymptotic behaviour of the VeLI shape ratio for a homogeneous shell	31
9	Viscoelastic isostasy for a shell with depth-dependent rheology: application to Enceladus and Europa	32

List of Tables

1	Internal structure parameters for a 3-layer body with homogeneous layers	12
2	Love numbers as a sum of fluid and deviatoric components	13
3	Laplace transforms	17
4	Equivalences between endmembers of elastic and dynamic approaches	33
5	High-degree asymptotic behaviour of Love number generic coefficients	41

1 Introduction

At large scale, most topography on Earth (bathymetry included) is in isostatic equilibrium, meaning that surface loads are buoyantly supported by subsurface mass anomalies, due to crustal thickness variations or density variations within the crust and lithosphere, in such a way that stresses are hydrostatic below a constant depth called the compensation depth [Phillips and Lambeck, 1980]. Textbook examples are the average depth of the oceans, the elevation of the Himalayas, and the subsidence of ocean floor away from midocean ridges, respectively explained by the thin oceanic crust (compared to thick continental crust), crustal thickening under mountain belts, and density increase due to plate cooling [Turcotte and Schubert, 2014; Fowler, 2005]. In general, the isostatic concept is applied very simply, by partitioning the crust into vertical columns floating independently in a fluid and in mechanical equilibrium. This picture is known to be oversimplified both at short and long wavelengths [Lambert, 1930; Jeffreys, 1932, 1943; Vening Meinesz, 1946; Dahlen, 1982]. While the short-scale issue can be handled by combining isostasy with lithospheric flexure (that is flexural isostasy), the large-scale inadequacy does not appear clearly in Earth data because mantle flow becomes the dominant factor in large-scale geoid anomalies [Hager *et al.*, 1985a,b]. Moreover the contribution of mantle flow to the long-wavelength shape (called dynamic topography) is comparable to isostatic topography [Hoggard *et al.*, 2016; Davies *et al.*, 2019; Flament, 2019].

On terrestrial-type planetary bodies, isostatic equilibrium occurs locally but has not yet been found to operate globally: geologic provinces with highly compensated gravity have been identified on Venus [Smrekar and Phillips, 1991; Simons *et al.*, 1997], Mars [McGovern *et al.*, 2002, 2004], and the Moon [Sori *et al.*, 2018]. Nevertheless, predictions of dynamic topography on Venus depend, as on Earth, on the computation of isostatic topography at long wavelengths (e.g. Pauer *et al.* [2006]). Isostasy found a new domain of application in icy satellites with subsurface oceans, where the ice-to-water transition embodies the isostatic requirement of a hydrostatic layer below the depth of compensation. Global isostasy thus seems likely in that setting; gravity data suggest that it operates on Enceladus [Iess *et al.*, 2014; McKinnon, 2015; Beuthe *et al.*, 2016; Hemingway *et al.*, 2018], Dione [Beuthe *et al.*, 2016; Zannoni *et al.*, 2020], and Titan [Durante *et al.*, 2019], whereas the case of Europa is not yet settled for lack of data [Nimmo and Bills, 2010]. On the dwarf planet Ceres, gravity and shape data suggest nearly global isostatic compensation, although the negative gravity-shape correlation at degree and order two is incompatible with global isostasy [Ermakov *et al.*, 2017; Park *et al.*, 2020]. Icy moons and dwarf planets thus raise again the question of defining isostasy at all scales.

Attempts at improving classical isostasy belong to three categories. The first one includes arguments that some models of classical isostasy are better than others. For example, Hemingway and Matsuyama [2017] argue that classical isostasy assuming equal lithostatic pressure at the compensation depth should be preferred to the most common model of equal mass columns, whereas Cadek *et al.* [2019a] claim that isostasy based on

a principle of equal weight is a better approximation. Since neither ‘equal pressure’ nor ‘equal weight’ isostasy can be derived from fundamental physical principles, the error of each model must be estimated by building a more complete model of isostasy (see *Beuthe* [2021], hereafter called Paper I). In the second category, isostasy is treated as a problem of elastic equilibrium, which is determined so that deviatoric stresses are minimized within the crust or lithosphere [*Jeffreys*, 1959; *Dahlen*, 1982; *Beuthe et al.*, 2016]. The concept of ‘minimum stress isostasy’ originates in the observation that isostasy is a natural state in the evolution of a mechanical system in response to an applied stress field, because a mechanical system will always tend to respond in such a manner as to minimize stress [*Phillips and Lambeck*, 1980]. Paper I implemented this idea by formulating isostasy as the response, fully described by Love numbers, of a thick elastic shell floating on a fluid layer to the combined action of surface and internal loads. In the third category, isostasy naturally arises from viscous relaxation.

A common feature of classical isostasy and minimum stress isostasy is that they avoid the question of the loading history. This feature is simultaneously an advantage, because the loading history is most often unknown, and a drawback, because it is not clear whether plausible physical processes can lead to that outcome, and whether the isostatic balance is stable. Faulting of a brittle lithosphere can contribute to isostasy, but it is more likely that isostatic deformations at depth are due to creep. It has long been known that a perturbed viscous layer above a less viscous layer first relaxes to a state looking like Airy isostatic balance (at least for long-wavelength perturbations), before decaying slowly to hydrostatic equilibrium [*Ramberg*, 1968; *Phillips and Lambeck*, 1980; *Solomon et al.*, 1982; *Zhong*, 1997]. Figure 1 shows an example of the relaxation of a degree-two perturbation on the dwarf planet Ceres. The body is modelled as a two-layer viscoelastic sphere, with a more viscous shell of density ρ_1 surrounding a less viscous mantle/core of density ρ_2 . The initial stage of elastic support is followed by a transition to Airy balance, in which the shape ratio (i.e. the ratio of the shape of the bottom of the shell to the surface shape) becomes constant and approximately equal to $-(\rho_2 - \rho_1)/\rho_1$. The system then slowly evolves toward hydrostatic equilibrium, unless the evolution is stopped at the intermediate isostatic stage because stresses have fallen below the creep threshold [*Phillips and Lambeck*, 1980].

In this context, Airy isostasy is a particular stage of the more general process of isostatic adjustment, which describes the time-dependent response of a planetary body to the modification of surface loads. On Earth, the best-known example of isostatic adjustment is the postglacial rebound of Scandinavia [*Steffen and Wu*, 2011], with similar rebounds occurring in Canada and Antarctica. These observed changes in surface elevation are now seen as one manifestation of Glacial Isostatic Adjustment (GIA) among others, such as global sea-level change, gravity field variations, fluctuations of the Earth’s rotation axis and length of day etc. (see reviews by *Mitrovica and Wahr* [2011] and *Whitehouse* [2018]; theoretical aspects are covered in *Sabadini et al.* [2016]). Given the abundance of time-dependent data (sea level, GPS, and gravity), it has become possible to build global models of glacial loading [e.g. *Peltier*, 2004; *Lambeck et al.*, 2014; *Peltier et al.*, 2015], constrain-

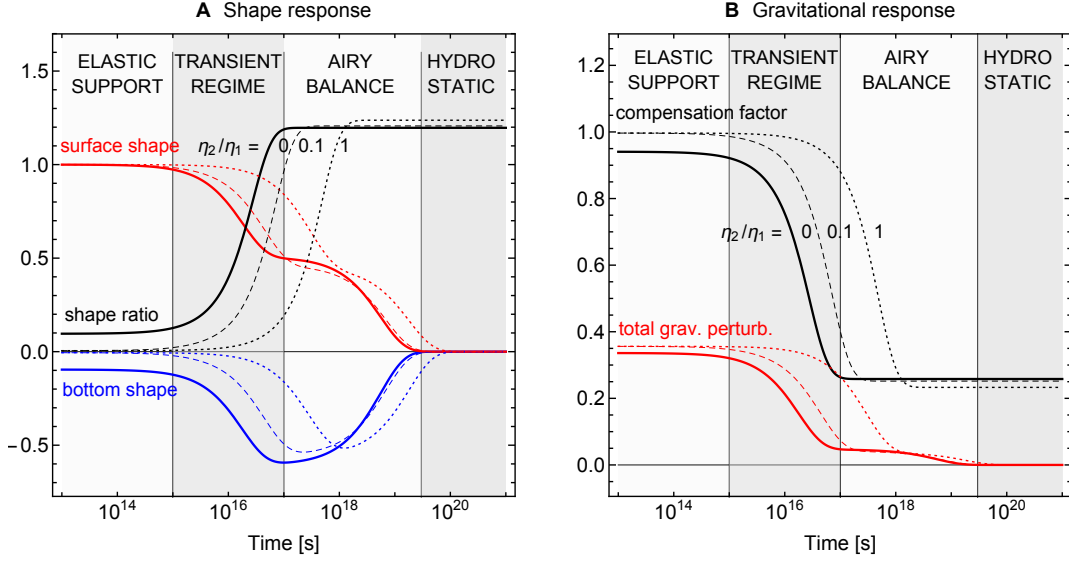


Figure 1: Viscoelastic relaxation of a two-layer spherical body: (A) shape of interfaces and shape ratio; (B) perturbation of gravitational potential and compensation factor. A degree-2 load is applied at the surface at $t = 0$ and remains constant. The shapes and the gravitational perturbation are normalized so that the initial surface shape is unity. The shape ratio (shown in absolute value) and compensation factor are defined in Section 2. The viscosities of the bottom and top layers are in the ratio $\eta_2/\eta_1 = 0$ (solid), 0.1 (dashed), or 1 (dotted). Shaded areas distinguish the four successive stages for the case of a fluid bottom layer ($\eta_2/\eta_1 = 0$): elastic support, transient regime, Airy balance, and hydrostatic equilibrium. This example is based on the two-layer Ceres model specified by $\rho_1 = 1286 \text{ kg/m}^3$; $\rho_2 = 2434 \text{ kg/m}^3$; $R_1 = 469.7 \text{ km}$; $R_2 = 428.8 \text{ km}$; $\mu_1 = 3.5 \text{ GPa}$; $\eta_1 = 10^{25} \text{ Pa}\cdot\text{s}$ [Ermakov et al., 2017].

ing at the same time the global sea level history [e.g. *Kopp et al.*, 2009] and the mantle viscosity [e.g. *Mitrovica*, 1996; *Lau et al.*, 2016]. Interior models have become complex, with viscosity varying not only with depth but also laterally [e.g. *A et al.*, 2013]. GIA data, however, are not sufficient to invert for lateral variations of viscosity, and a priori knowledge about them is lacking [*Whitehouse*, 2018].

Beyond Earth, isostatic adjustment of impact craters and basins (and sometimes the global shape) is widely used to constrain the rheology of planets and moons. Following early works [*Parmentier and Head*, 1981; *Solomon et al.*, 1982; *Passey*, 1983; *Grimm and Solomon*, 1988; *Thomas and Squyres*, 1988], topographic relaxation is now systematically studied on all large bodies of the solar system: the Moon [*Zhong and Zuber*, 2000; *Mohit and Phillips*, 2006; *Kamata et al.*, 2012, 2013; *Qin et al.*, 2018], Mars [*Zhong*, 2002; *Pathare et al.*, 2005; *Mohit and Phillips*, 2007], Mercury [*Mohit et al.*, 2009], dwarf planets [*Fu et al.*, 2014; *Bland et al.*, 2016; *Ermakov et al.*, 2017; *Fu et al.*, 2017; *Sori et al.*, 2017], Galilean satellites [*Dombard and McKinnon*, 2000, 2006; *Bland et al.*, 2017], and Saturnian satellites [*Robuchon et al.*, 2011; *Bland et al.*, 2012; *White et al.*, 2013, 2017].

In the theory of isostatic adjustment, isostasy refers to the initial state (before loading or unloading) and to the final stationary state reached after an infinite time. The infinite time response of the system for a step function load is called ‘isostatic response’ and results in the ‘final state of isostatic equilibrium’ which is hydrostatic unless an elastic lithosphere provides static support [*Peltier*, 1974; *Peltier*, 1976; *Wu and Peltier*, 1982; *Han and Wahr*, 1995; *Cambiotti et al.*, 2013]. This terminology, however, excludes from isostasy the intermediate stage of Airy isostatic balance illustrated in Figure 1. By contrast, the present work addresses long-term processes that have reached this particular stage where the shape ratio has become stationary. As shown in Figure 1, Airy isostatic balance, once achieved, is not very sensitive to the viscosity ratio between the sublayer and the shell as long as the shell has a higher viscosity. The system can thus be modelled as a viscoelastic shell above an inviscid sublayer, as done by *Ermakov et al.* [2017]. In that case, the average viscosity of the shell does not affect Airy isostasy, but the variation of rheology with depth does (lateral variations are ignored for simplicity). This assumption allows me to keep the model as close as possible to the traditional concept of isostasy, as well as to the elastic equilibrium approach. This complements the work of *Zhong and Zuber* [2000], who studied the appearance of isostatic equilibrium in configurations where the layers are either viscous or elastic (see also *Zhong* [1997, 2002]), and the one of *Kamata et al.* [2012], who computed the long-term relaxation of stratified bodies with time-dependent viscosity.

Although viscous relaxation is an attractive mechanism to produce Airy isostasy, the lower viscosity at the bottom of the shell can lead to strong lateral flow which destroys the isostatic topography [*Gratton*, 1989; *Bird*, 1991; *McKenzie et al.*, 2000]. The problem is particularly acute for icy satellites with subsurface oceans, because of the short relaxation time scale at the shell-ocean boundary which results from the low viscosity of ice at melting point and the free-slip condition at the interface. Topography can instead be maintained in a dynamical equilibrium if nonuniform internal heating causes uneven melting/freezing

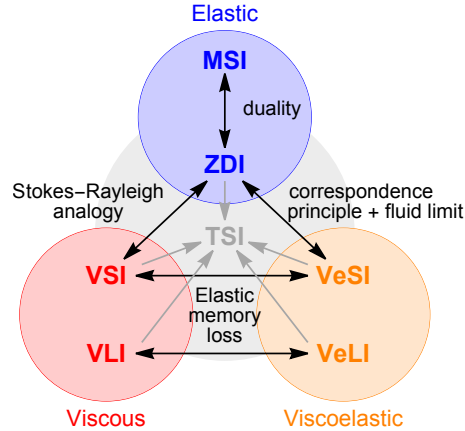


Figure 2: Relations between elastic, viscoelastic, and viscous isostatic models. The acronyms stand for minimum stress isostasy (MSI), zero deflection isostasy (ZDI), viscoelastic ‘constant shape’ isostasy (VeSI), viscoelastic ‘constant load’ isostasy (VeLI), viscous ‘constant shape’ isostasy (VSI), viscous ‘constant load’ isostasy (VLI). In the thin shell limit, all models tend to thin shell isostasy (TSI).

at the bottom of the shell [Kamata and Nimmo, 2017; Cadek et al., 2017; Kvorka et al., 2018; Cadek et al., 2019a,b]. At long wavelengths, nonuniform heating is produced by tidal dissipation within the shell or the core. If the satellite is at equilibrium, tidal dissipation is constant so that the melting/freezing rate is constant too. In the Love number approach, this corresponds to a load increasing linearly with time, whose lateral flow results in a shell of constant shape. Global equilibrium between tidally dissipated heat and heat loss through conduction or convection is a plausible outcome for a satellite in orbital resonance [Segatz et al., 1988; Fuller et al., 2016; Nimmo et al., 2018]. However, the thermal-orbital evolution can also display oscillations around equilibrium [Ojakangas and Stevenson, 1986; Fischer and Spohn, 1990; Hussmann and Spohn, 2004; Meyer and Wisdom, 2008], in which case the load and the shape both depend on time. For these reasons, I will examine Airy isostasy with variable loads, focussing on the case of constant shape, but considering also more general time-dependent loads.

In this paper, I extend the ‘Isostasy with Love’ framework of Paper I in order to describe Airy isostasy as resulting from viscoelastic relaxation. The viscoelastic and viscous approaches are in principle equivalent in the long time limit, as there is no memory left of the initial elastic response. While this equivalence seems natural in the time-dependent approach, in which the load is not modified after emplacement, it is less obvious in the stationary approach, in which the load evolves with time in order to maintain the boundary condition. We thus have (too) many isostatic approaches based on sound physical principles: minimum elastic stress, viscoelastic evolution, and viscous evolution, with the two last ones in time-dependent and stationary versions.

In Paper I, I showed that the invariance of elastic isostasy under a global rescaling of the shear modulus means that it can be computed in the fluid limit. This property also suggests a connection with the asymptotic state of a viscoelastic/viscous shell. Similarly, viscoelastic isostasy is invariant under a global rescaling of viscosity, the counterpart of the fluid limit being the long-time limit. If the shell is homogeneous, elastic and viscoelastic isostatic models actually depend on the same set of interior parameters. Using the correspondence principle and the fluid limit, I will establish an exact relation between stationary viscoelastic isostasy and elastic isostasy; more general time-dependent loads will be shown to result in a similar Airy isostatic balance. Besides, I will use the Stokes-Rayleigh analogy to relate stationary viscous isostasy to elastic isostasy. By contrast, the time-dependent versions of viscoelastic and viscous isostasy are equivalent between them, but differ from the stationary version. Fig. 2 illustrates the relations between elastic, viscoelastic, and viscous approaches. Existing isostatic models thus belong to two independent groups: the elastic/stationary approaches, and the time-dependent approaches. In the thin shell limit, all models yield the same predictions which coincide with the thin shell model of *Dahlen* [1982]. At high harmonic degree, shell thickness matters and the various models give slightly different predictions of geoid anomalies.

Viscoelastic Love numbers can be computed with standard methods [*Sabadini et al.*, 2016] and various software packages [*Spada et al.*, 2011], although the latter should be modified to include forcing by internal loads. Airy isostasy *stricto sensu* corresponds to the case of a shell of uniform rheology, but I will also discuss shells with depth-dependent rheology which are particularly relevant for icy moons with subsurface oceans [*Cadek et al.*, 2019a]. Fully analytical solutions are feasible for simple configurations, and are given in the complementary software for a 3-layer incompressible body with homogeneous layers [*Beuthe*, 2020].

2 Isostatic ratios in terms of deviatoric Love numbers

2.1 Loading the shell

In Paper I, Airy isostasy was formulated as an elastic loading problem, more precisely as the mechanical equilibrium of loads applied at the surface and at the bottom of the shell. The theoretical framework is the same in viscoelastic isostasy, except that the shell is now viscoelastic. Besides, surface and internal loads do not need to be both present since mechanical balance results from viscoelastic relaxation. This section summarizes formulas that are readily applicable to viscoelastic isostasy, whereas Appendix A includes those that are specific to elastic isostasy.

The initial state, or unperturbed model, is spherically symmetric with a viscoelastic shell (or crust) floating on a fluid layer (ocean or asthenosphere) surrounding an elastic core (see Table 1). Surface and internal loads, respectively associated with the initial elevations of the surface ($H_n^{L,init}$) and shell-ocean boundary ($H_n^{I,init}$), are applied to the shell

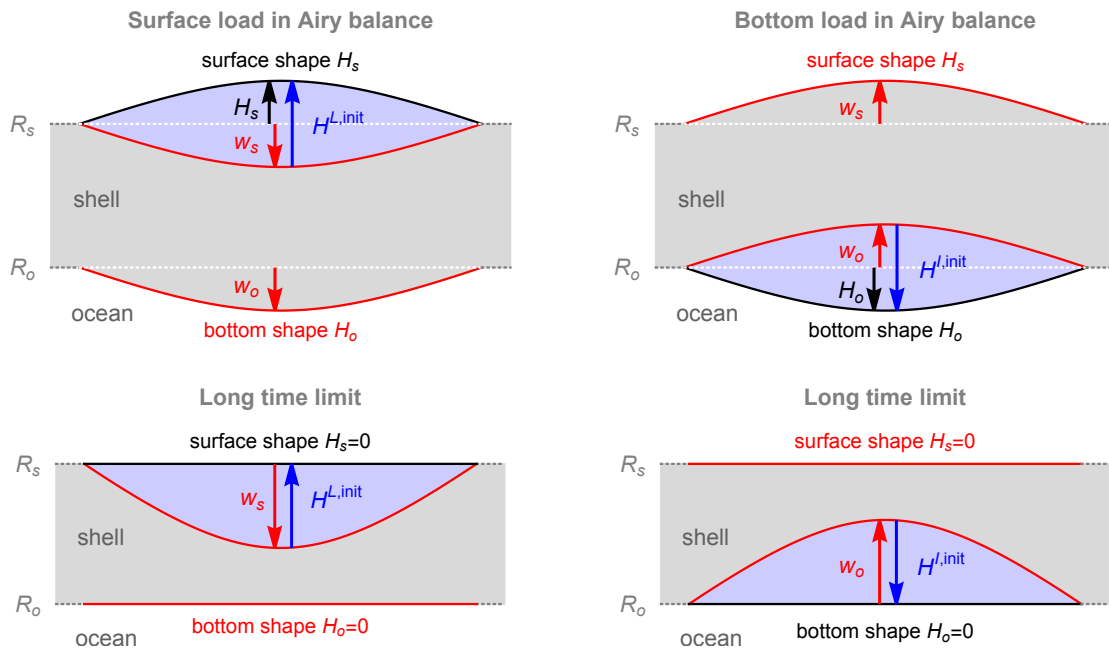


Figure 3: Loading of a viscoelastic shell by a surface load (left panels) or a bottom load (right panels). The top row shows the stage of Airy isostatic balance while the bottom row shows the long time limit. In these examples, the shell is thickened by the load. The ocean density is twice the shell density.

which responds by deforming and perturbing the initial gravity field (Fig. 3). The equations of equilibrium and Poisson’s equation are linearized around the unperturbed state under the assumption that loads and deformations have a small amplitude. Shape and gravitational perturbations are expanded in spherical harmonics with degree $n \geq 2$. At degree 1, the shape perturbation is fully compensated in the centre-of-mass frame (Section 3.3 of Paper I). By analogy with tidal forcing, the topographic loading is represented by the gravitational potentials produced by the initial elevations at the radii where they are located:

$$H_n^{L,init} = \frac{1}{\xi_{sn}} \frac{U_n^L}{g_s}, \quad (1)$$

$$H_n^{I,init} = \frac{1}{x\Delta\xi_n} \frac{U_n^I}{g_s}, \quad (2)$$

with parameters defined in Table 1. These formulas depend on the Airy assumption that the surface and internal loads are defined by undulations of the shell boundaries with respect to their unperturbed spherical state, so that the associated surface mass densities are $\rho_s H_n^{L,init}$ and $(\rho_o - \rho_s) H_n^{I,init}$, respectively. According to potential theory (see Eqs. (7)-(8) of Paper I), the gravitational perturbations due to the combined loads at the shell boundaries are given by

$$\Gamma_{sn}^{\text{direct}} = U_n^L + x^{n+1} U_n^I, \quad (3)$$

$$\Gamma_{on}^{\text{direct}} = x^n U_n^L + U_n^I. \quad (4)$$

The superscript ‘direct’ denotes that the contribution due to the deformation of the body is not included.

Radial Love numbers (h_j^L, h_j^I) relate the radial deformation of the shell boundaries (excluding the load, as in Fig. 3) to the load potentials:

$$w_{jn} = \frac{1}{g_s} (h_j^L U_n^L + h_j^I U_n^I). \quad (5)$$

The indices $j = (s, o)$ label the top and bottom of the shell (s for surface and o for ocean). Gravitational Love numbers (k_j^L, k_j^I) do the same job for the gravitational perturbation induced by the deformation of the body:

$$\Gamma_{jn}^{\text{induced}} = k_j^L U_n^L + k_j^I U_n^I. \quad (6)$$

However, we are neither interested by the deformation nor by the induced gravity, which are not observable, but instead by the shape of the shell boundaries (H_{sn}, H_{on}) and the total gravitational perturbation at the same interfaces (Γ_{sn}, Γ_{on}). The former are the sum of the initial elevation (‘direct effect’) and the radial deformation, while the latter are the sum of direct and induced gravitational contributions. The direct effects can be written

Table 1: Internal structure parameters for a 3-layer body with homogeneous layers.

Parameter	Symbol	Nondimensional version
Surface (or shell) radius	R_s	1
Ocean (or asthenosphere) radius	R_o	$x = R_o/R_s$
Shell thickness	d_s	$\varepsilon = d_s/R_s = 1 - x$
Bulk density	ρ_b	1
Shell density	ρ_s	$\xi_{sn} = \frac{3}{2n+1} (\rho_s/\rho_b)$
Ocean density	ρ_o	$\xi_{on} = \frac{3}{2n+1} (\rho_o/\rho_b)$
Density contrast (ocean-shell)	$\rho_o - \rho_s$	$\Delta\xi_n = \xi_{on} - \xi_{sn}$
Surface gravity	g_s	$\gamma_s = 1$
Gravity at bottom of shell	g_o	$\gamma_o = g_o/g_s = (1 + (x^3 - 1)\xi_{s1})/x^2$
Elastic shear modulus (shell)	μ_s	$\bar{\mu}_s = \mu_s/(\rho_b g_s R_s)$

in terms of the negative of the *fluid Love numbers* ($h_j^{J^\circ}, k_j^{J^\circ}$) given in Table 2, so that the shape and total gravitational perturbation read

$$H_{jn} = (-h_j^{L^\circ} + h_j^L) \frac{U_n^L}{g_s} + (-h_j^{I^\circ} + h_j^I) \frac{U_n^I}{g_s}, \quad (7)$$

$$\Gamma_{jn} = (-k_j^{L^\circ} + k_j^L) U_n^L + (-k_j^{I^\circ} + k_j^I) U_n^I. \quad (8)$$

Fluid Love numbers were computed in Paper I from the elastic-gravitational equations; they are not sensitive to the deep interior (below the shell). If there is no elastic lithosphere, the shell tends in the long time limit to a fluid state and Love numbers tend to their fluid values, so that the shape of the shell boundaries and the total gravitational perturbation both vanish (Fig. 3). The vanishing of the shape depends on the Airy assumption that loads are defined by undulations of the shell boundaries (Eqs. (1)-(2)).

It is convenient to define *deviatoric Love numbers* which vanish in the long time (or fluid) limit:

$$\hat{h}_j^J = h_j^J - h_j^{J^\circ}, \quad (9)$$

$$\hat{k}_j^J = k_j^J - k_j^{J^\circ}, \quad (10)$$

where $j = (s, o)$ and $J = (L, I)$. The shape and total gravitational perturbation can then be written in terms of load potentials and deviatoric Love numbers:

$$H_{jn} = \frac{1}{g_s} \left(\hat{h}_j^L U_n^L + \hat{h}_j^I U_n^I \right), \quad (11)$$

$$\Gamma_{jn} = \hat{k}_j^L U_n^L + \hat{k}_j^I U_n^I. \quad (12)$$

These formulas make it explicit that the shape and the total gravitational perturbation vanish in the long time (or fluid) limit, together with the deviatoric Love numbers.

Table 2: Radial Love numbers h_j^J and gravitational Love numbers k_j^J (implicitly at harmonic degree n) as a sum of fluid and deviatoric (‘Dev’) components. The superscript denotes the forcing (L for surface load; I for internal load); the subscript denotes the interface where the Love number is evaluated (s for top of shell; o for bottom of shell).

Radial			Gravitational		
Full	Fluid	Dev.	Full	Fluid	Dev.
h_j^J	$h_j^{J\circ}$	\hat{h}_j^J	k_j^J	$k_j^{J\circ}$	\hat{k}_j^J
h_s^L	$-1/\xi_{sn}$	\hat{h}_s^L	k_s^L	-1	\hat{k}_s^L
h_o^L	0	\hat{h}_o^L	k_o^L	$-x^n$	\hat{k}_o^L
h_s^I	0	\hat{h}_s^I	k_s^I	$-x^{n+1}$	\hat{k}_s^I
h_o^I	$-1/(x\Delta\xi_n)$	\hat{h}_o^I	k_o^I	-1	\hat{k}_o^I

2.2 Isostatic ratios

Isostatic ratios are nondimensional quantities characterizing the output of an isostatic model. They depend on deviatoric Love numbers and on the *loading ratio* which is the ratio of the internal load to the surface load:

$$\zeta_n = U_n^I/U_n^L. \quad (13)$$

In elastic isostasy, the loading ratio is determined by the choice of the isostatic prescription (e.g. minimum stress), but it is a free parameter in viscoelastic isostasy, for which arbitrary loads can be applied at the surface and at the bottom of the shell. It is not a priori clear whether viscoelastic isostasy depends or not on the loading ratio.

Shape and gravitational perturbations (Eqs. (11)-(12)) can be combined into various nondimensional isostatic ratios, the most important of which is the *compensation factor* F_n , defined as the ratio of the geoid perturbation Γ_{sn}/g_s to the surface shape H_{sn} , normalized so that F_n varies between 0 (full compensation) and 1 (no compensation):

$$F_n = \frac{1}{\xi_{sn}} \frac{\Gamma_{sn}}{g_s H_{sn}} = \frac{1}{\xi_{sn}} \frac{\hat{k}_s^L + \zeta_n \hat{k}_s^I}{\hat{h}_s^L + \zeta_n \hat{h}_s^I}. \quad (14)$$

Its importance comes from the fact that it can be computed from quantities observable at the surface. By contrast, the *shape ratio* S_n and the *topographic ratio* T_n are not easily

observable, but are useful proxies when constructing new isostatic models:

$$S_n = \frac{H_{on}}{H_{sn}} = \frac{\hat{h}_o^L + \zeta_n \hat{h}_o^I}{\hat{h}_s^L + \zeta_n \hat{h}_s^I}, \quad (15)$$

$$T_n = \frac{H_{on} - \Gamma_{on}/g_o}{H_{sn} - \Gamma_{sn}/g_s} = \frac{1}{\gamma_o} \frac{\hat{t}_o^L + \zeta_n \hat{t}_o^I}{\hat{t}_s^L + \zeta_n \hat{t}_s^I}, \quad (16)$$

where $\hat{t}_j^J = \gamma_j \hat{h}_j^J - \hat{k}_j^J$. If the body is incompressible and the density of the shell is uniform, gravitational Love numbers can be computed in terms of radial Love numbers at the shell boundaries. In that case, isostatic ratios are related by

$$S_n = \frac{(1-a)(\gamma_o T_n) + c}{b(\gamma_o T_n) + d}, \quad (17)$$

$$\xi_{sn} F_n = b S_n + a, \quad (18)$$

with (a, b, c, d) given in Table 3 of Paper I.

3 Viscoelastic isostasy

3.1 Time-dependent Love numbers

In the viscoelastic approach, the shell initially at hydrostatic equilibrium is loaded at time $t = 0$ by surface and bottom loads with some constant loading ratio ζ_n^V . If the viscosity of the shell is not infinite, the system evolves with time towards hydrostatic equilibrium. As the shell flows away under the loads, the internal stresses decrease and the shell finds itself in a state of approximate equilibrium, or isostatic balance: the shapes of the top and bottom shell boundaries tend to zero, but their ratio is constant (Fig. 4). The shape ratio and compensation factors are thus defined for viscoelastic isostasy by the long-time limit of Eqs. (14)-(15) in which Love numbers depend on time:

$$F_n = \lim_{t \rightarrow \infty} \frac{1}{\xi_{sn}} \frac{\hat{k}_s^L(t) + \zeta_n^V \hat{k}_s^I(t)}{\hat{h}_s^L(t) + \zeta_n^V \hat{h}_s^I(t)}, \quad (19)$$

$$S_n = \lim_{t \rightarrow \infty} \frac{\hat{h}_o^L(t) + \zeta_n^V \hat{h}_o^I(t)}{\hat{h}_s^L(t) + \zeta_n^V \hat{h}_s^I(t)}, \quad (20)$$

where ζ_n^V denotes the loading ratio in viscoelastic isostasy. If the load evolves in time, its time-dependence is included in the time-dependent Love numbers (see Eq. (30) and Section 3.4). Recall that the topographic ratio and compensation factor can be computed from the shape ratio if the body is incompressible and the shell of uniform density (Eqs. (17)-(18)).

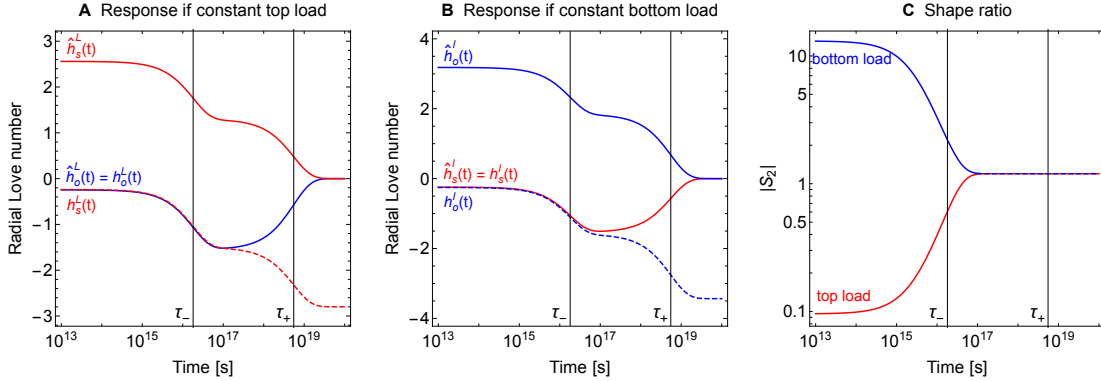


Figure 4: Radial displacement of shell boundaries under a constant degree-two load, as a function of time: (A) top load; (B) bottom load; (C) absolute value of shape ratio. This example is based on the two-layer Ceres model of *Ermakov et al.* [2017] (see Fig. 1). The deformation of the top and bottom shapes (including the load) is quantified by the deviatoric Love number (solid curves), which tends to zero in the long time limit. The deformation of the interface between shell and load is quantified by the full Love number (dashed curves). Red and blue curves correspond to the top and bottom of the shell, respectively. Vertical lines indicate the two viscoelastic decay times ($\tau_- = 1.80 \times 10^{16}$ s and $\tau_+ = 5.52 \times 10^{18}$ s).

3.2 Correspondence principle

The principle of correspondence [*Peltier, 1974*] gives a practical procedure to compute time-dependent Love numbers of a viscoelastic body:

1. compute the solution of the elastic problem;
2. replace the elastic shear modulus μ_e by the s -dependent function $\tilde{\mu}(s)$ characterizing the rheology, s being the Laplace domain variable;
3. multiply the result by the Laplace transform $\tilde{T}(s)$ of the time history of the load;
4. take the inverse Laplace transform of this transformed solution (see Table 3).

For Maxwell rheology, the shear modulus in the Laplace domain reads

$$\tilde{\mu}(s) = \frac{\mu_e s}{s + \mu_e/\eta}, \quad (21)$$

where μ_e is the elastic shear modulus and η is the viscosity (see *Peltier* [1982] for other rheological models). In the large- s limit, the material is purely elastic; in the small- s limit, it looks like a fluid with an asymptotic behaviour governed by the viscosity:

$$\lim_{s \rightarrow \infty} \tilde{\mu}(s) = \mu_e, \quad (22)$$

$$\lim_{s \rightarrow 0} \tilde{\mu}(s) = 0, \quad (23)$$

$$\partial_s \tilde{\mu}(s) \Big|_{s=0} = \eta. \quad (24)$$

I will now explain how viscoelastic Love numbers are related to their elastic, fluid, and deviatoric components. Equations are given below for radial Love numbers, but similar equations hold for gravitational Love numbers. In the Laplace domain (in which functions are denoted with a tilde), Love numbers can be written as a sum over normal modes of viscous gravitational relaxation [Peltier, 1976; Wu and Peltier, 1982; Sabadini *et al.*, 2016].

$$\tilde{h}_j^J(s) = h_{je}^J + \sum_p \frac{r_{jp}^J}{s - s_p}, \quad (25)$$

where h_{je}^J is the elastic Love number (it does not depend on s) and r_{jp}^J are the residues associated with the poles $s = s_p$ which are on the negative real axis ($s_p < 0$). Since the poles are the eigenvalues of the homogeneous viscoelastic-gravitational problem, they do not depend on the type of loading and are also poles for the gravitational Love numbers. The simplest interior model appropriate for isostasy (incompressible body with homogeneous shell, inviscid ocean, and elastic core) has two modes because there is one viscoelastic layer (the shell) which has two boundaries with a density contrast (see Section 1.8 of Sabadini *et al.* [2016]).

In the large- s limit, Laplace-domain Love numbers tend to their elastic values:

$$\lim_{s \rightarrow \infty} \tilde{h}_j^J(s) = h_{je}^J. \quad (26)$$

In the small- s limit, they tend to their fluid values (Table 2):

$$\begin{aligned} \lim_{s \rightarrow 0} \tilde{h}_j^J(s) &= h_{je}^J - \sum_p \frac{r_{jp}^J}{s_p} \\ &= h_j^{J^\circ}. \end{aligned} \quad (27)$$

The remainder is the deviatoric component which vanishes in the small- s limit:

$$\begin{aligned} \hat{h}_j^J(s) &= \tilde{h}_j^J(s) - h_j^{J^\circ} \\ &= \sum_p \frac{r_{jp}^J}{s_p} \frac{s}{s - s_p}. \end{aligned} \quad (28)$$

In analogy with Eq. (A.2), the partial derivative of the Laplace-domain Love number with respect to s and evaluated at $s = 0$ is denoted

$$\begin{aligned} \dot{\hat{h}}_j^J &= \partial_s \tilde{h}_j^J(s) \Big|_{s=0} \\ &= - \sum_p \frac{r_{jp}^J}{(s_p)^2}. \end{aligned} \quad (29)$$

In order to go over to the time domain, I must specify the time history of the load. Given the Laplace transform $\tilde{T}(s)$ of the loading time history, the final value theorem [Peltier, 1974; Dyke, 2014] relates the long-time limit of the time-dependent Love number to the small- s limit of its Laplace transform:

$$\lim_{t \rightarrow \infty} \hat{h}_j^J(t) = \lim_{s \rightarrow 0} s \left(\tilde{T}(s) \hat{h}_j^J(s) \right). \quad (30)$$

Table 3: Laplace transforms used in this paper. The first two columns give the time dependence of the load and its Laplace transform; the last two columns give the inverse Laplace transform of the product of the load with the function $f(s) = s/(s - a)$ (a is real and negative) and its asymptotic behaviour at large times. $u(t)$ denotes the unit step function; q is a positive integer; $\Gamma(q)$ and $\Gamma(q, a)$ are the gamma function and the incomplete gamma function, respectively.

$T(t)$	$\tilde{T}(s)$	$\mathcal{L}^{-1}(\tilde{T}(s) f(s))$	$t \rightarrow \infty$
$u(t)$	$1/s$	$\exp(at) u(t)$	$\exp(at)$
$u(t - t_1)$	$\exp(-t_1 s)/s$	$\exp(a(t - t_1)) u(t - t_1)$	$\exp(a(t - t_1))$
$t u(t)$	$1/s^2$	$a^{-1}(\exp(at) - 1)u(t)$	$-1/a$
$t^q u(t)$	$\Gamma(q + 1)/s^{q+1}$	$q a^{-q} \exp(at)(\Gamma(q) - \Gamma(q, at)) u(t)$	$(-q/a) t^{q-1}$
$\cos(\omega t)u(t)$	$s/(s^2 + \omega^2)$	$\frac{a^2 \exp(at) + \omega^2 \cos(\omega t) + a\omega \sin(\omega t)}{a^2 + \omega^2} u(t)$	$\frac{\omega^2 \cos(\omega t) + a\omega \sin(\omega t)}{a^2 + \omega^2}$

3.3 Constant load

Constant loading means that the load applied at $t = 0$ remains constant beyond some threshold $t_0 > 0$. This model is relevant to the relaxation of topography that is not modified after its emplacement, for example small-scale features such as craters and dormant volcanoes, or large-scale loads such as the fossil figure due to faster rotation in the past. Since any continuous loading history can be approximated by a series of discrete steps [Peltier, 1976], it is usual to start with the simpler case of a surface (or internal) load brought from infinity at time $t = 0$ and remaining constant for $t > 0$. The time history of this load is represented by the Heaviside (or unit step) function $u(t)$, the Laplace transform of which is $\tilde{T}(s) = 1/s$ (see Table 3). The final value theorem implies that the long time limit of the deviatoric Love number is equal to the small- s limit of the Laplace-domain deviatoric Love number, which vanishes:

$$\lim_{t \rightarrow \infty} \hat{h}_j^J(t) \Big|_{\text{VeLI}} = \hat{h}_j^J(0) = 0, \quad (31)$$

where ‘VeLI’ stands for **V**isco-elastic (constant) **L**oad **I**sostasy. This equation is not sufficient to compute the shape ratio and compensation factor which have the indeterminate

form 0/0. One needs to know precisely how the deviatoric Love number decreases as s tends to zero. For this purpose, I compute the inverse Laplace transform of the product of Eq. (28) and $\tilde{T}(s) = 1/s$ (see Table 3):

$$\hat{h}_j^J(t)\Big|_{\text{VeLI}} = \sum_p \frac{r_{jp}^J}{s_p} \exp(s_p t) u(t). \quad (32)$$

In order to facilitate comparisons with *Peltier* [1976], I also give the time evolution of the full Love number (for $t > 0$):

$$h_j^J(t)\Big|_{\text{VeLI}} = h_{je}^J + \sum_p \frac{r_{jp}^J}{s_p} \left(\exp(s_p t) - 1 \right). \quad (33)$$

In the long-time limit, the time evolution of the Love number is given by the exponential term with the longest time scale: $\tau_+ = -1/s_+$, where s_+ denotes the pole closest to zero. The shape ratio is thus equal to the ratio of the long time-scale residues:

$$S_n^{\text{VeLI}} = \frac{r_{o+}^L + \zeta_n^V r_{o+}^I}{r_{s+}^L + \zeta_n^V r_{s+}^I}. \quad (34)$$

The VeLI shape ratio does not depend on the loading ratio because

$$S_n^{\text{VeLI}} = \frac{r_{o+}^L}{r_{s+}^L} = \frac{r_{o+}^I}{r_{s+}^I}. \quad (35)$$

This property is implied by the μ -invariance of elastic isostasy (see Eq. (B.15)).

The compensation factor is computed in the same way. The result can be written as

$$F_n^{\text{VeLI}} = \frac{1}{\xi_{sn}} \frac{r_{s+}^L + \zeta_n^V r_{s+}^I}{r_{s+}^L + \zeta_n^V r_{s+}^I}, \quad (36)$$

where r_{j+}^J are the long time-scale residues for gravitational Love numbers. It is simpler, however, to compute F_n from S_n with Eq. (18) if the body is incompressible and the shell is of uniform density. As for the shape ratio, the VeLI compensation factor does not depend on the loading ratio.

More complicated loading histories (but constant for $t > t_0$) can be approximated by a series of unit steps starting at different times $0 < t_1 < t_2 < \dots < t_0$. A unit step load shifted at time $t = t_1$ has the effect of translating the result in the time domain (see Table 3), so that Eq. (32) is multiplied by $\exp(-s_p t_1)$. Such factors drop out of VeLI isostatic ratios, which are thus unaffected by the non-constant loading prior to the threshold $t = t_0$. As expected, the isostatic balance keeps no memory of its early loading history.

Suppose now that the body is incompressible, the shell is homogenous, and the core is elastic (including the limiting cases of a fluid or an infinitely rigid core). In that case,

there are only two relaxation modes (see Appendix B.1): Love numbers evolve in time as superpositions of a short-time decay mode, corresponding to the shell boundaries moving in the same direction, and a long-time decay mode, corresponding to shell boundaries moving in opposite directions, as shown by the solid curves in Fig. 4 (the same feature occurs in the viscous model, see *Hager and O'Connell [1979]*). Assuming that the ocean and the core are homogeneous, I derive in Appendix B analytical formulas for the decay times and the shape ratio in terms of generic Love number coefficients. Among several equivalent expressions (Eqs. (B.13)-(B.17)), the shape ratio is for example given by

$$S_n^{\text{VeLI}} = \frac{F\mu_+ - \xi_{sn} B_s^L}{x\Delta\xi_n B_s^I}, \quad (37)$$

where the Love number coefficients (B_s^L, B_s^I, F) and the pole μ_+ are defined by Eqs. (B.1) and (B.6). The analytical formulas are coded in the complementary software.

The VeLI isostatic ratios have the following general properties:

1. They are independent of the position of the load (at surface or at shell-ocean interface); more generally, they are independent of the loading ratio (Eq. (35)).
2. They do not depend on the elastic properties of the shell (elastic memory loss). They should thus be identical to the isostatic ratios of viscous isostasy with constant load (see Section 4.4).
3. They do not change if the viscosity of the shell is rescaled by a global factor (ν -invariance). They are thus independent of the viscosity of the shell if it is uniform (see Eqs. (B.13)-(B.14)).
4. They have the same thin shell limit as elastic isostasy (Eqs. (A.9) and (B.22)-(B.23)).
5. At high harmonic degree, the shape ratio for a homogeneous shell diverges to $-\infty$ if $\psi = \gamma_o x\Delta\xi_1/\xi_{s1} \leq 1$ (the most physically plausible case); it tends to zero if $\psi > 1$ (Eqs. (B.25)-(B.26)). The compensation factor for a homogeneous shell does not diverge.

The viscoelastic-viscous equivalence does not extend to decay times which are somewhat affected by the elastic shear modulus, but the discrepancy is small for the longest decay time (Eqs. (B.9)-(B.10)). In the thin shell limit, the longest relaxation time ($\tau_+ = -1/s_+$) can be approximated from Eqs. (B.19) and (B.21),

$$\tau_+ \cong \frac{\eta}{\rho_s g_s d} \frac{2(2n^2 + 2n - 1)}{n(n+1)} \frac{\xi_{o1}}{\Delta\xi_1}, \quad (38)$$

which agrees with the prediction of the viscous flow model in Cartesian geometry, taken in the thin shell limit: $\tau_+ \cong (4\eta/\rho_s g_s d)(\rho_o/(\rho_o - \rho_s))$ (see Eq. (A33) of *Solomon et al. [1982]*).

3.4 Constant shape

Consider now loading with constant shape, either at the surface or at the shell-ocean interface. In the long-time limit, the final value theorem (Eq. (30)) shows that the time-dependent deviatoric Love number tends to a non-zero constant if $\tilde{T}(s) = 1/s^2$, which corresponds to a load increasing linearly with time (see Table 3). For example, the melting (of the shell) or freezing (of the ocean) due to a constant heat flux from below can be interpreted as a bottom load increasing linearly with time. For ‘constant shape’ loading, the long-time limit of the deviatoric Love number is thus given by

$$\lim_{t \rightarrow \infty} \hat{h}_j^J(t) \Big|_{\text{VeSI}} = - \sum_p \frac{r_{jp}^J}{(s_p)^2} = \dot{h}_j^J, \quad (39)$$

where the last equality results from Eq. (29) and ‘VeSI’ stands for **V**isco-elastic (constant) **S**hape **I**sostasy. The shape ratio is thus given by a formula very similar to the one obtained in the fluid limit of elastic isostasy (Eq. (A.1)), except that partial derivatives are evaluated in the Laplace domain:

$$S_n^{\text{VeSI}} = \frac{\dot{h}_o^L + \zeta_n^V \dot{h}_o^I}{\dot{h}_s^L + \zeta_n^V \dot{h}_s^I}. \quad (40)$$

Suppose now that the shell has a Maxwell rheology (or another rheology which is fluid-like in the long term) and is stratified into N layers with viscosities (η_1, \dots, η_N) . Using the correspondence principle and the chain rule, I relate the partial derivative of the Laplace-domain Love number to the partial derivative of the Love number of an elastic body with a shell stratified into N layers with shear moduli (μ_1, \dots, μ_N) :

$$\begin{aligned} \dot{h}_j^J &= \sum_{i=1}^N \left(\frac{\partial}{\partial \mu_i} h_{je}^J \right) \left(\frac{\partial}{\partial s} \tilde{\mu}_i(s) \right) \Big|_{s=0} \\ &= \eta_0 \sum_{i=1}^N \frac{\eta_i}{\eta_0} \frac{\partial}{\partial \mu_i} h_{je}^J \Big|_{\mu_1=0 \dots \mu_N=0}. \end{aligned} \quad (41)$$

The elastic shear moduli of the viscoelastic model play no role in this expression because Eq. (24) depends only on the viscosity. Eq. (41) looks very much like the partial derivative of the elastic Love number in the fluid limit (Eq. (A.3)). It can indeed be written as

$$\dot{h}_j^J = \eta_0 \dot{h}_j^J, \quad (42)$$

if the elastic shell in the RHS has a depth-dependent elastic shear modulus varying in the same way as the viscosity of the viscoelastic model in the LHS:

$$\frac{\eta_i}{\eta_0} = \frac{\mu_i}{\mu_0}. \quad (43)$$

In that case, the formulas for the shape ratio and compensation factor have the same form as those of elastic isostasy in the fluid limit (Eq. (A.1)) with the substitution $\zeta_n^o \rightarrow \zeta_n^V$:

$$S_n^{\text{VeSI}} = \frac{\dot{h}_o^L + \zeta_n^V \dot{h}_o^I}{\dot{h}_s^L + \zeta_n^V \dot{h}_s^I}. \quad (44)$$

Thus, ‘constant shape’ viscoelastic isostasy gives the same result as zero-deflection isostasy (ZDI) if ζ_n^V coincides with the corresponding fluid loading ratio (Eq. (A.4)):

$$\zeta_n^V = -\frac{\Delta\xi_1}{\xi_{s1}} \frac{x}{\alpha}. \quad (45)$$

Therefore, ‘constant shape’ viscoelastic isostasy with purely surface loading ($\zeta_n^V = 0$) is equivalent to elastic isostasy with zero deflection at the shell-ocean boundary ($\alpha = \infty$). Conversely, ‘constant shape’ viscoelastic isostasy with purely bottom loading ($\zeta_n^V = \pm\infty$) is equivalent to elastic isostasy with zero deflection at the surface ($\alpha = 0$). If the body is incompressible and has a homogeneous shell, the shape ratio can be expressed in terms of generic coefficients of Love numbers, as in Eq. (A.7):

$$S_n^{\text{VeSI}} = -\frac{\xi_{s1}}{x\Delta\xi_1} \frac{B_o^L - (\xi_{s1}/x\Delta\xi_1) \zeta_n^V B_s^L}{B_o^I - (\xi_{s1}/x\Delta\xi_1) \zeta_n^V B_s^I}. \quad (46)$$

This formula is coded in the complementary software.

The VeSI isostatic ratios have the following properties:

1. They depend on the position of the load (at surface or at shell-ocean interface); more generally, they depend on the loading ratio ζ_n^V .
2. They do not depend on the elastic properties of the shell (elastic memory loss). They should thus be identical to the isostatic ratios of viscous isostasy with constant shape (see Section 4.5).
3. They are ν -invariant, meaning that they do not change if the viscosity of the shell is rescaled by a global factor. They are thus independent of the viscosity of the shell if it is uniform.
4. They have the same thin shell limit as elastic isostasy (Eq. (A.9)) and as viscoelastic isostasy with constant load. In other words, boundary conditions do not matter in the thin shell limit.
5. At high harmonic degree, the shape ratio for a homogeneous shell tends to zero for pure top loading whereas it diverges to $-\infty$ for pure bottom loading (Eqs. (B.27)-(B.28)). The compensation factor does not diverge.

3.5 Variable load and shape

Is isostatic balance still possible for loads that are neither constant nor proportional to time? In the long time limit, isostatic balance can be approximately satisfied, or not at all, depending on whether the load variation is slower or faster than the time scale of viscoelastic relaxation. As a first example, consider loading with polynomial time dependence $T(t) \sim t^q$ (see Table 3), of which the ‘constant shape’ model is a special case ($q = 1$). In the long time limit, the deviatoric Love number behaves as

$$\hat{h}_j^J(t) \sim -\frac{t^{q-1}}{\Gamma(q)} \sum_p \frac{r_{jp}^J}{(s_p)^2}, \quad (47)$$

which is proportional to the ‘constant shape’ value (Eq. (39)). The resulting isostatic ratios are identical to those of the ‘constant shape’ model. Thus, the ‘constant shape’ isostatic balance generally holds for loads with polynomial time dependence, which vary more slowly (in the long time limit) than viscoelastic exponential decay.

A more realistic model is a load with periodic time dependence $T(t) \sim \cos(\omega t)$ (see Table 3), which could result from the oscillation of the orbital eccentricity [*Ojakangas and Stevenson, 1986; Meyer and Wisdom, 2008*]. In the long time limit, the deviatoric Love number behaves as

$$\hat{h}_j^J(t) \sim \sum_p \frac{r_{jp}^J}{s_p} \frac{\omega}{s_p^2 + \omega^2} (\omega \cos(\omega t) + s_p \sin(\omega t)). \quad (48)$$

If the load varies much more slowly than the viscoelastic timescale ($\omega \ll |s_p|$), then the deviatoric Love number is well approximated in the long time limit by

$$\hat{h}_j^J(t) \sim \omega \sin(\omega t) \sum_p \frac{r_{jp}^J}{(s_p)^2}. \quad (49)$$

In that case, the isostatic ratios are identical to those of the ‘constant shape’ model.

4 Viscous isostasy

4.1 Slow viscous flow

The theory of slow viscous flow describes flows in which the fluid is incompressible, isothermal, and has a rheology with no memory of a past elastic response [*Ribe, 2015*]. It has been widely applied – with stationary boundary conditions – to study plate dynamics, mantle convection, and geoid anomalies (*Hager and O’Connell [1979]; Richards and Hager [1984]; Ricard et al. [1984]*; earlier work is reviewed by *Hager and O’Connell [1978]*). Beside these stationary models, slow viscous flows have been used to compute time-dependent

post-glacial rebound on Earth [*Hager and O’Connell, 1979*] and the relaxation of impact basins on planetary bodies [*Solomon et al., 1982*]. Two recent applications are directly relevant to the computation of isostatic ratios: the time-dependent approach used by *Er-makov et al. [2017]* for Ceres, which is based on the propagator matrix method of *Hager and Clayton [1989]*, and the stationary model proposed by *Cadek et al. [2019a]* for Enceladus, which they solve with their own semi-analytical (spectral) methods and fully numerical (finite-element) methods.

4.2 Stokes-Rayleigh analogy

The fluid limit of elastic isostasy (Appendix A) suggests that it does not differ that much from viscoelastic or viscous relaxation. There is actually a precise mathematical correspondence, called the Stokes-Rayleigh analogy, between the theory of small incompressible elastic deformations and the theory of slow viscous flows [*Ribe, 2015*]. The constitutive equations of the two theories are related by the following exchanges:

$$\begin{aligned} \text{displacements} &\leftrightarrow \text{velocities,} \\ \text{shear modulus} &\leftrightarrow \text{viscosity.} \end{aligned}$$

This correspondence is not readily apparent when these theories are formulated in linearized form (as sets of 6 differential equations of first order in the propagator matrix approach), because the equations of motion involving viscous and elastic stresses are derived in Eulerian and Lagrangian descriptions, respectively [*Wang, 1997*].

Beyond the governing equations, the Stokes-Rayleigh analogy also applies to the solutions to boundary value problems if the boundary conditions themselves are analogous [*Ribe, 2018*]. In the case of interest here, the Stokes-Rayleigh analogy predicts for an incompressible body that elastic isostasy with zero surface (resp. bottom) deflection is equivalent to ‘constant shape’ viscous isostasy with zero surface (resp. bottom) radial velocity.

4.3 Propagator matrix approach

The theory of slow viscous flow is very similar in structure to the gravitational-elastic equations used to compute Love numbers, with the important difference that displacement and strain variables are replaced by velocity and strain rate variables (this correspondence is discussed in Section 4.2). In the formulation of *Hager and Clayton [1989]*, there are 6 first-order differential equations for the radial and tangential velocities, the radial and radial-tangential stresses, and the gravitational potential and its derivative. The problem is solved by propagating the variables at the bottom of the viscous shell to the surface, and by imposing the appropriate boundary conditions at both interfaces. *Hager and Clayton [1989]* do not give explicitly the propagator for the velocity and stress variables (suggesting to compute it with Sylvester’s formula), while their propagator for the gravity variables is printed with typos. For these reasons, and also to emphasize the similarity of the viscous

formalism with the gravitational-elastic theory, I show in Appendix C how to compute the propagator matrices as two-point products of the so-called fundamental matrices. Moreover, the boundary conditions on (Eulerian) stress and gravity variables are not always explicit or appear with some typos in *Hager and Clayton* [1989]; I give them in correct form in Appendix C. An implicit assumption of the viscous approach of *Hager and Clayton* [1989] is that there is no perturbation due to a deformable solid core.

The procedure described in Appendix C.5 yields two equations (or reduced propagation system) for the radial velocities ($u_1(R_s), u_1(R_o)$) and the radial displacements ($\delta r_s, \delta r_o$). If the shell is homogeneous, a fully analytical solution is feasible (see complementary software). In that case, the reduced propagation system has nondimensional coefficients which do not depend on viscosity if displacement variables are normalized as

$$\delta \bar{r}_j = \delta r_j / \tau_s \quad (j = s, o), \quad (50)$$

where the time scale $\tau_s = \eta_s / (\rho_b g_s R_s)$ is defined in terms of the uniform viscosity η_s .

If the rheology of the shell depends on depth, the problem can be solved numerically with the propagator matrix method by modelling the shell as a superposition of homogeneous thin spherical layers. The reduced propagation system is nondimensionalized as above, except that η_s is now an arbitrarily chosen viscosity (for example the viscosity at the surface). Moreover, the reduced propagation system is independent of the reference viscosity η_0 introduced for normalization purposes in the defining matrix \mathbf{A} (Eq. (C.3)).

4.4 Constant load

Similarly to viscoelastic isostasy, viscous isostasy can be solved for different loading histories. If the load is constant, the positions of the boundaries depend on time, as done for glacial unloading by *Hager and O'Connell* [1979] and for the isostatic shape ratio by *Ermakov et al.* [2017]. The condition of zero radial velocity imposed by *Hager and Clayton* [1989] is thus not appropriate here. Instead, the radial velocity of the flow is set equal to the time-derivative of the radial displacement:

$$u_1(R_s) = \frac{\partial}{\partial t}(\tau_s \delta \bar{r}_s) \quad \text{and} \quad u_1(R_o) = \frac{\partial}{\partial t}(\tau_s \delta \bar{r}_o). \quad (51)$$

With these conditions, the reduced propagation system can be written as a system of two coupled homogeneous differential equations of the first order for the time-dependent functions $\delta r_s(t)$ and $\delta r_o(t)$:

$$\tau_s \frac{\partial}{\partial t} \begin{pmatrix} \delta \bar{r}_s(t) \\ \delta \bar{r}_o(t) \end{pmatrix} = \mathbf{M} \cdot \begin{pmatrix} \delta \bar{r}_s(t) \\ \delta \bar{r}_o(t) \end{pmatrix}, \quad (52)$$

where \mathbf{M} is a 2×2 matrix depending on nondimensional parameters (it does not depend on viscosity if the shell is homogeneous). For example, the parameters for a homogeneous

shell can be chosen as $(x, \xi_{s1}, \xi_{o1}, n)$. Eq. (52) has two independent solutions given by

$$\begin{pmatrix} \delta\bar{r}_s(t) \\ \delta\bar{r}_o(t) \end{pmatrix} = \begin{pmatrix} w_{s\pm} \\ w_{o\pm} \end{pmatrix} \exp(\lambda_{\pm}t/\tau_s), \quad (53)$$

where λ_{\pm} and $\mathbf{w}_{\pm} = (w_{s\pm} \ w_{o\pm})$ are the eigenvalues and eigenvectors of \mathbf{M} , with $\lambda_- < \lambda_+ < 0$. The short $(-)$ and long $(+)$ decay times are given by

$$\tau_{\pm} = -\tau_s/\lambda_{\pm}. \quad (54)$$

At large times ($t \gg \tau_s/|\lambda_-|$), the solution with the most negative eigenvalue λ_- becomes negligible and the shape ratio tends to a constant:

$$S_n^{\text{VLI}} = \lim_{t \rightarrow \infty} \frac{\delta\bar{r}_o(t)}{\delta\bar{r}_s(t)} = \frac{w_{o+}}{w_{s+}}, \quad (55)$$

where ‘VLI’ stands for **V**iscous (constant) **L**oad **I**sostasy. If the shell is homogeneous, this method yields analytical formulas for the decay times and the shape ratio, which depend on the nondimensional parameters $(x, \xi_{s1}, \xi_{so}, n)$, but not on viscosity. Assuming an incompressible body, I show in the complementary software that these formulas are identical to the ‘constant load’ viscoelastic isostatic ratios of Section 3.3. They also agree perfectly with the numerical results of *Ermakov et al.* [2017] (see Fig. 5).

4.5 Constant shape

For Enceladus, *Cadek et al.* [2019a] assume that the shape of the shell-ocean boundary is maintained by melting or freezing due to heat flow from below the shell. This shape cannot be identified with the bottom boundary of the viscous layer, because there is a continuous transfer of material between the shell and the ocean. One can impose, however, that the surface shape does not change with time (since there is no transfer of material there) or, equivalently, that the radial velocity of the surface vanishes:

$$u_1(R_s) = 0. \quad (56)$$

In that model, the radial velocity at the bottom corresponds to the radial velocity of the ice flow, which does not vanish but is compensated by the formation or melting of ice. Contrary to the case of constant load, the velocity of the flow at the bottom boundary is not directly related to the radial displacement. The reduced propagation system of Appendix C.5 can be written as two coupled inhomogeneous equations in the variables $(u_1(R_o), \delta\bar{r}_o)$ with an inhomogeneous term proportional to $\delta\bar{r}_s$ (it can be set equal to 1). Once this system has been solved, the isostatic shape ratio is given by

$$S_n^{\text{VSI}} = \frac{\delta\bar{r}_o}{\delta\bar{r}_s}, \quad (57)$$

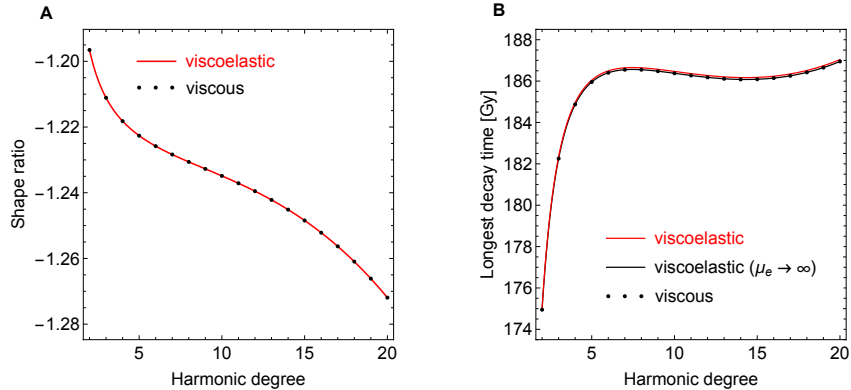


Figure 5: Viscoelastic/viscous isostasy with constant load: benchmarking against the solution of *Ermakov et al.* [2017]. The two panels show the shape ratio and the longest decay time as a function of harmonic degree. Parameters are the same as in Fig. 1. Solid red curves show the predictions of viscoelastic isostasy; black dots are the predictions of viscous isostasy. Predictions for the shape ratio are analytically (and numerically) the same in the two approaches. Viscoelastic decay times are slightly affected by the elastic shear modulus μ_e , but become identical to viscous decay times in the limit of large μ_e (only the longest decay time is shown).

where ‘VSI’ stands for **V**iscous (constant) **S**hape **I**sostasy. If the shell is homogeneous, the shape ratio does not depend on the uniform viscosity of the shell. If the shell is stratified into thin layers of homogeneous rheology, the shape ratio depends on the ratios of the viscosities of the different layers, but is invariant under an overall rescaling of the shell viscosity. This property of η -invariance mirrors the property of μ -invariance for elastic isostasy.

For an incompressible body, the VSI shape ratio given by Eq. (57) is analytically equivalent to the VeSI shape ratio with purely bottom loading (see complementary software). Therefore, it is equivalent to the shape ratio of elastic isostasy with zero deflection at the surface, exactly as predicted by the Stokes-Rayleigh analogy (Section 4.2). Mathematically, it is possible to define viscous isostasy with zero velocity at the shell-ocean boundary, although the physical interpretation is not obvious. The linear combination of the two extreme boundary conditions results in a 1-parameter isostatic family which is equivalent to the 1-parameter family of zero-deflection elastic isostasy.

Finally, the results obtained with the propagator matrix method described here agree perfectly with the results of *Cadek et al.* [2019a] (more precisely those obtained with the spectral method), whether the shell has a constant or variable viscosity (Fig. 6). If the shell has a depth-dependent viscosity, the equivalent elastic model consists in a shell having a shear modulus that depends on depth in the same way as the viscosity in the viscous model (note that the overall scale of the shear modulus does not matter because of μ -invariance).

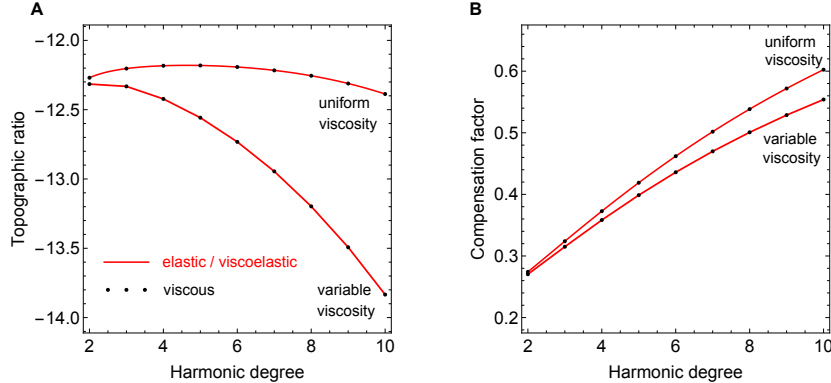


Figure 6: Elastic/viscoelastic/viscous isostasy with constant shape: benchmarking against the solution of *Cadek et al.* [2019a]. The two panels show the topographic ratio and the compensation factor as a function of harmonic degree. The 3-layer model of Enceladus is specified by $\rho_s = 926 \text{ kg/m}^3$, $\rho_o = 1010 \text{ kg/m}^3$, $d = 20 \text{ km}$, $R_s = 252.1 \text{ km}$, and a non-deformable core with density 2366 kg/m^3 and radius 194 km . Viscoelastic isostasy is computed from elastic isostasy with no surface deflection ($\alpha = 0$) given by Eq. (A.8) if viscosity is uniform; the variable viscosity case is solved numerically with the elastic propagator matrix method [Sabadini et al., 2016]. Viscous isostasy is solved with the viscous propagator matrix method (Section 4.5). For clarity, the elastic/viscoelastic solution is shown as a continuous curve.

Fig. 6 shows that this procedure yields the same results as the viscous propagator method.

5 Application to Enceladus and Europa

5.1 Interior models and computational methods

As in Paper I, I consider Enceladus and Europa as example cases of isostasy. Both bodies harbour an internal ocean but differ significantly in their shell thickness: Enceladus has a thick shell ($d_s \sim 8$ to 12% of R_s), whereas Europa has a thin shell ($d_s \sim 1$ to 5% of R_s). The interior model for Enceladus is specified by $\rho_s = 920 \text{ kg/m}^3$; $\rho_o = 1020 \text{ kg/m}^3$; $\rho_b = 1610 \text{ kg/m}^3$; $d = 23 \text{ km}$; $R_s = 252.1 \text{ km}$ [Beuthe et al., 2016]. For Europa, I adopt the same shell density, ocean density, and shell thickness as for Enceladus; the bulk density and the surface radius are $\rho_b = 3013 \text{ kg/m}^3$ and $R_s = 1560.8 \text{ km}$. The core is infinitely rigid in both cases.

I will first assume that the shell is of uniform viscosity, in which case viscosity drops out of the isostatic ratios and analytical formulas are available (see complementary software). This model corresponds closely to what is traditionally viewed as Airy isostasy. I will then examine the more realistic case of a shell with depth-dependent rheology (the

‘constant shape’ case was previously studied by *Cadek et al.* [2019a]; see Fig. 6). In that case, isostatic ratios are affected by viscosity variations but do not depend on the overall magnitude of viscosity. This model must be solved numerically. Stationary viscoelastic isostasy is equivalent to ZDI elastic isostasy and can thus be solved with the propagator matrix method for elastic Love numbers [*Sabadini et al.*, 2016] or, alternatively, with the viscous propagator method of Section 4.5. Time-dependent isostasy can be solved either by computing Love number residues [*Peltier*, 1985; *Jara-Oru e and Vermeersen*, 2011; *Sabadini et al.*, 2016] or with the viscous propagator method of Section 4.4.

5.2 Uniform viscosity

Fig. 7 shows the viscoelastic shape ratio and compensation factor for Enceladus and Europa as a function of harmonic degree if their shell is of uniform viscosity. Predictions of viscoelastic isostasy with ‘constant load’ (VeLI) or ‘constant shape’ (VeSI) are indistinguishable at low harmonic degree and are well approximated in that range by thin shell isostasy (using the ‘improved’ version of thin shell isostasy discussed after Eq. (A.9)). As harmonic degree increases, the shape ratio diverges for VeLI as well as for VeSI-bottom (that is VeSI with bottom loading, which is the physically relevant case). At high harmonic degree, VeLI remains close to VeSI-bottom if the shell-ocean density contrast is small, whereas VeLI diverges more slowly if the density contrast is large (as in the Ceres model of Fig. 5). This statement can be made more precise by studying the asymptotic behaviour of the shape ratio at high harmonic degree (see Appendix B.5). For a 3-layer incompressible body with homogeneous layers, S_n^{VeLI} typically tends to a constant fraction of $S_n^{\text{VeSI,bot}}$ (Fig. 8). As in elastic isostasy, the divergence of the VeSI-bottom shape ratio at high harmonic degree can be explained by “Jeffreys’ theorem” [*Melosh*, 2011]: loads are supported by stresses over a radial distance of about $R_s/n \approx \lambda/2\pi$ where λ is the load wavelength (see Fig. 9 of Paper I). Since a bottom load of small extent is supported by stresses close to the bottom of the shell, it does not induce stresses close to the surface and the surface shape gets smaller, compared to the bottom shape, as the wavelength gets shorter.

The divergence of the VeLI and VeSI-bottom shape ratios is much faster if the shell is thicker (compare left and right panels of Fig. 7). Simply put, the predictions for Europa look like the predictions for Enceladus at a smaller harmonic degree. As expected, loads are more compensated (F_n closer to zero) at a given harmonic degree if the shell is thin.

Given that the viscosity is uniform, the VeSI/VSI-bottom model is equivalent to elastic isostasy with zero surface deflection in a shell with uniform shear modulus, which is in turn nearly identical to elastic isostasy based on minimum stress with the bottom shape kept constant during minimization (thick blue curves in Fig. 7). It is more natural, however, to keep the surface shape constant during minimization since it is more readily observable than the bottom boundary (thin blue curves in Fig. 7). In that case, the predictions of the VeSI/VSI-bottom model differ from those of minimum stress isostasy. Nevertheless, the

difference is only significant at short wavelengths where little Airy compensation occurs.

Predictions of classical isostasy are significantly off at long wavelengths, especially for the compensation factor (Fig. 7, panels E and F). In classical isostasy, the shape ratio varies little with the harmonic degree, which is a common feature of isostasy based on local compensation (that is, vertical columns move independently).

5.3 Depth-dependent rheology

At first sight, icy satellites with subsurface oceans provide a perfect setting for Airy isostasy, because the fluid layer below the compensation depth is not just an idealization but a fact. Complications however arise because such an icy shell cannot be approximated as homogeneous: the bottom of the shell is close to the melting temperature of ice and has thus a soft rheology, whereas the top of the shell is extremely cold and thus nearly rigid. Following *Beuthe* [2018, 2019], I assume that the shell is in a conductive state with conductivity inversely proportional to temperature. For a shell of thickness d without internal heat production, the temperature T at depth z from the surface is given by $T/T_s = (T_m/T_s)^{z/d}$ (spherical corrections are neglected), where T_m is the melting temperature (273 K) at the base of the shell and T_s is the mean surface equilibrium temperature (59 K for Enceladus and 100 K for Europa). The viscosity of ice is related to temperature by an Arrhenius relation: $\eta = \eta_m \exp(E_a(1/T - 1/T_m))/R_g$, where $\eta_m = 10^{14}$ Pa.s is the viscosity at the melting temperature, $E_a = 59.4$ kJ mol⁻¹ is the activation energy for diffusion creep, and R_g is the gas constant. Close to the melting temperature, this rudimentary model is only a rough approximation of a much more complex picture [*Goldsby and Kohlstedt*, 2001]. At low temperatures, laboratory constraints are lacking [*Durham and Stern*, 2001] and it is customary (for numerical convenience) to impose a viscosity cutoff in the range 10^{20} to 10^{30} Pa.s.

Fig. 9 shows the VeLI and VeSI-bottom shape ratio and compensation factor for Enceladus and Europa as a function of harmonic degree. If the load is constant, isostatic ratios are radically affected by the depth-dependent rheology: Airy compensation becomes negligible at all wavelengths if the viscosity cutoff is high enough ($10^{24} - 10^{26}$ Pa.s). If the bottom shape is constant, the shape ratio diverges faster with harmonic degree than for a shell of uniform viscosity, confirming what *Cadek et al.* [2019a] found for the topographic ratio (see Fig. 6). The shape ratio even becomes singular at a finite value of the harmonic degree. Beyond that threshold, surface topography of positive amplitude cannot be supported by a stationary buoyant root at the bottom of the shell: Airy isostasy breaks down. Nevertheless, the predictions of VeSI-bottom remain close to the uniform viscosity model at low harmonic degrees where the mechanism of heat transfer maintaining a stationary shape is the most plausible (less than 20% deviation if $n \leq 10$ for Enceladus and $n \leq 50$ for Europa).

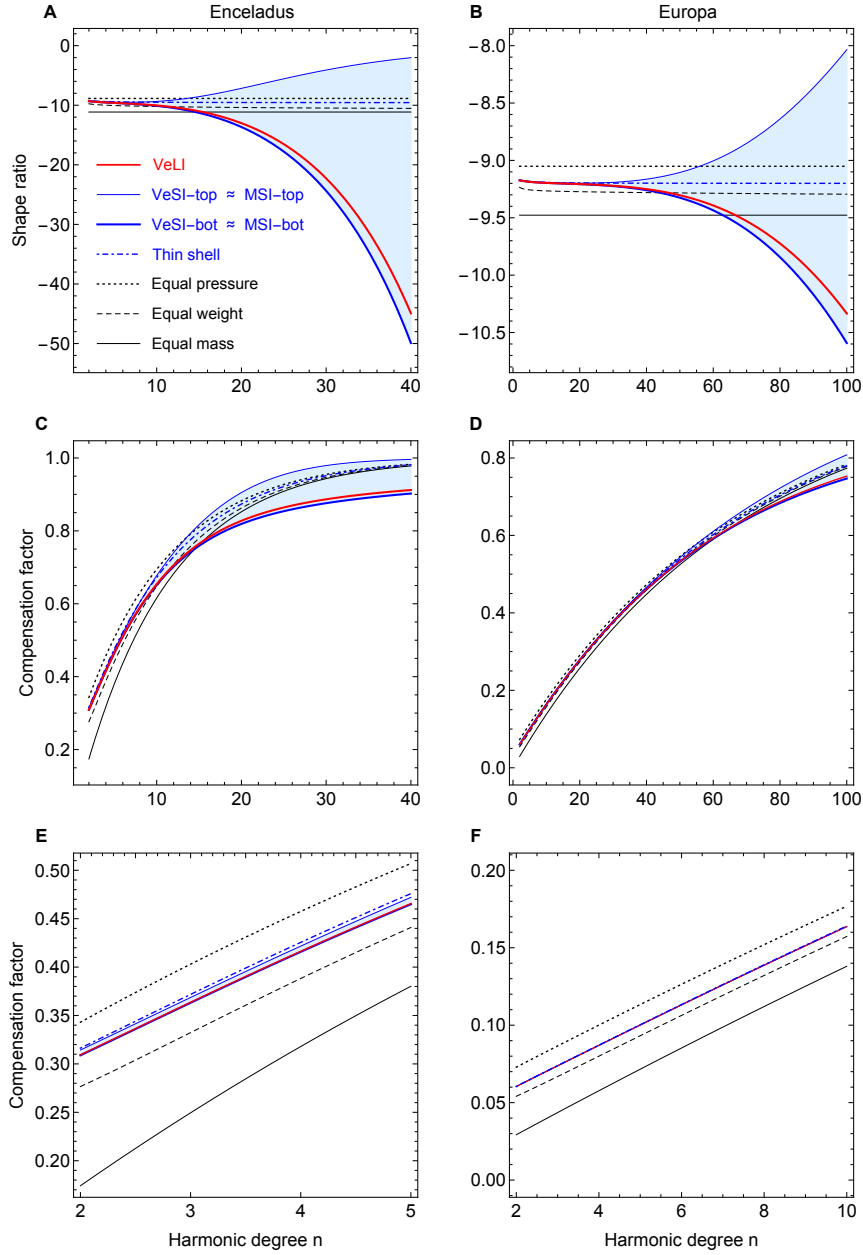


Figure 7: Viscoelastic isostasy for a homogeneous shell: shape ratio (first row) and compensation factor (second and third rows), as a function of harmonic degree, for Enceladus (left) and Europa (right). Lower panels zoom on the lower harmonic degrees of the middle panels. Red curves show ‘constant load’ viscoelastic isostasy (VeLI). Blue curves show ‘constant shape’ viscoelastic isostasy (VeSI), with thick and thin curves corresponding to bottom (= bot) and top loading, respectively. The shaded area represents combined top and bottom loading. The connection to minimum stress isostasy (MSI) is discussed in the text. Various models of classical isostasy are shown as thin black curves: equal pressure (dotted), equal weight (dashed), equal mass (solid). ‘Improved’ thin shell isostasy (see after Eq. (A.9)) is shown as a dash-dotted blue curve. Interior models are specified in Section 5.1.

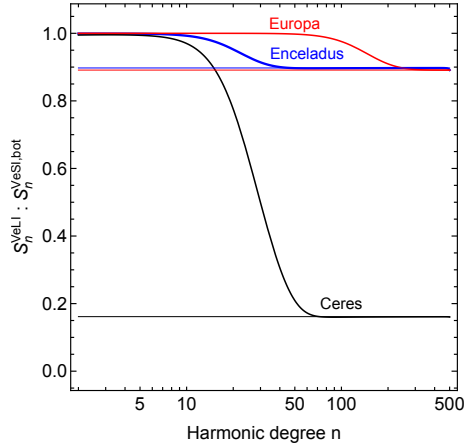


Figure 8: Asymptotic behaviour of the VeLI shape ratio for a homogeneous shell. At high harmonic degree, the VeLI shape ratio tends to a constant fraction of the VeSI shape ratio. The constant fraction (shown as thin horizontal lines) is equal to $1 - \gamma_o x \Delta \xi_1 / \xi_{s1}$ (Eq. (B.29)).

6 Conclusions

The application of Airy isostasy to a planet or moon at the global scale requires going beyond the classical picture of vertical columns floating in a fluid. For this purpose, two kinds of new isostatic models have been developed: they are based, on the one hand, on static elastic equilibrium minimizing the crustal stress and, on the other, on dynamic equilibrium realized through time-dependent or stationary viscous flow. After studying elastic models in Paper I, I have examined in this sequel dynamic models of isostasy and how they can be related to elastic isostasy. Among the various possible loading histories, two dynamic models stand out by their close connection to realistic scenarios. In the first one, a constant load is applied at the surface. This model describes topography that was emplaced in the past and has relaxed to a state of Airy balance, for example a crater or a dormant volcano. In the second model, a time-dependent load is applied at the bottom of the shell so that the shape of the shell boundaries remains constant. This stationary model corresponds to a dynamic equilibrium between viscous flow and melting/freezing at the bottom of the shell due to heat transfer between shell and ocean. If heat is generated by tidal heating, it is likely that such an equilibrium mainly occurs at the longest wavelengths (harmonic degrees 2 and 4), although turbulence could result in melting/freezing variations of shorter wavelength if the ocean transports heat from the core to the shell. The stationary model can be extended to scenarios where both load and shape vary slowly, as is the case if the thermal-orbital evolution of a satellite in a resonance falls into an oscillating pattern.

The first key result of this paper is to establish equivalences, wherever they exist, between elastic, viscoelastic, and viscous approaches to isostasy. Fig. 2 and Table 4 summarize the results. First, viscoelastic and viscous approaches do not differ at all. Second,

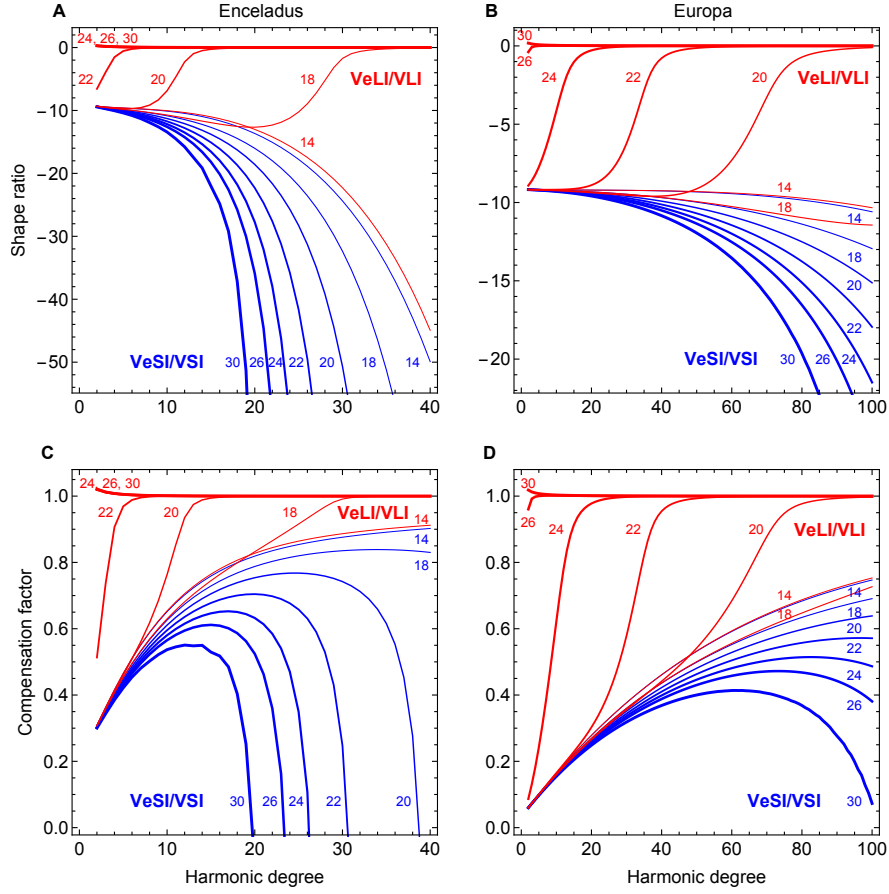


Figure 9: Viscoelastic isostasy for a shell with depth-dependent rheology: shape ratio (first row) and compensation factor (second row), as a function of harmonic degree, for Enceladus (left) and Europa (right). Red curves show isostasy with constant load (VeLI or VLI) whereas blue curves show isostasy with constant bottom shape (VeSI or VSI). The bottom viscosity is 10^{14} Pa.s. The thickness of the curve increases with the cutoff on the maximum viscosity η_{cut} (labeled by $\log_{10}(\eta_{\text{cut}})$). The label ‘14’ corresponds to a homogeneous shell as on Fig. 7. Interior models of Enceladus and Europa are the same as in Fig. 7; the rheology is specified in Section 5.3.

Table 4: Equivalences between three endmembers of elastic and dynamic approaches to isostasy. Equivalent models are grouped in three rows.

	Elastic isostasy	Elastic isostasy	Viscoelastic isostasy	Viscous isostasy
1	zero deflection no surface deflection $\alpha = 0$	minimum stress bottom shape nearly fixed $\beta = \alpha_0 \ll 0$ (*)	constant shape increasing bottom load $\zeta_n^V = \pm\infty$	stationary (constant shape) no mass exchange at surface $u_1(R_s) = 0$
2	zero deflection no bottom deflection $\alpha = \pm\infty$	minimum stress surface shape nearly fixed $\beta = \alpha_\infty \approx 0$ (*)	constant shape increasing surface load $\zeta_n^V = 0$	stationary (constant shape) no mass exchange at bottom $u_1(R_o) = 0$
3	no elastic equivalent – –	no elastic equivalent – –	constant load time-dependent shape loading ratio is irrelevant	time-dependent (constant load) no mass exchange at all unique boundary conditions

(*) duality based on the homogeneous shell assumption (Eq. (A.6)).

stationary viscoelastic/viscous isostasy is mathematically equivalent to zero-deflection elastic isostasy. Third, for each model of stationary viscoelastic/viscous isostasy (assuming a homogeneous shell), one can find an equivalent model of minimum stress elastic isostasy, although the boundary conditions (given by ζ_n^V and β) are connected in a non-trivial way by the $\alpha - \beta$ duality discussed in Paper I.

Thanks to these equivalences, stationary dynamic isostasy can be solved indifferently with elastic, viscoelastic, or viscous methods, depending on the user’s preferences. For time-dependent dynamic isostasy, searching for all the normal modes associated with Love numbers is probably not the most efficient method, since only the mode with the longest decay time is relevant to isostasy. On the other hand, such codes have been developed to a high degree of sophistication for post-glacial rebound studies. In the end, the choice of the method is more a question of software availability and personal experience. For the viscous approach, I gave a new formulation of the propagation matrix in terms of the fundamental matrix, similar to what is done when computing elastic or viscoelastic Love numbers of an incompressible body stratified in homogeneous layers. The viscous propagator matrices and the boundary conditions are fully implemented in the complementary software.

The existence of these equivalences teaches us two things. On the one hand, the freedom to define a new isostatic model is limited: isostatic approaches based on different physical principles (elastic equilibrium or viscoelastic relaxation) yield exactly the same isostatic ratios if boundary conditions correspond (Table 4), and share the same thin shell limit whatever the boundary conditions (contrary to classical isostasy). On the other, it shows that boundary conditions matter. Isostatic ratios usually differ if boundary conditions are applied at the surface or at the bottom of the shell, with the exception of dynamic isostasy with constant load. This difference, which is most notable in the shape ratio (Fig. 7,

panels A and B), increases with harmonic degree and with shell thickness, and depends on the assumption of isotropic elasticity (the difference is negligible if compensation is local). It can be explained by the migration of supporting stresses closer to the applied load (“Jeffreys’ theorem”). Predictions for the compensation factor are not very sensitive to the choice of boundary conditions if the shell is homogeneous (Fig. 7, panels C to F). If the rheology depends strongly on depth, one must think first about choosing the correct boundary conditions applicable to the problem and the harmonic degree range in which they are valid (Fig. 9).

The second key result of this paper is to provide analytical formulas for viscoelastic/viscous isostasy, with either constant load or constant shape, for an incompressible 3-layer model with homogeneous layers (see code in *Beuthe* [2020]). It is thus not justified anymore (at least at long wavelengths) to work with classical isostasy formulas just because they are simpler. If the shell is not of uniform viscosity, the analytical formulas can be used to benchmark the numerical codes used to compute isostatic ratios.

Acknowledgments

I thank Anton Ermakov and Ondrej Cadek for stimulating discussions which inspired this paper. I also thank Isamu Matsuyama and Bert Vermeersen for constructive comments about the manuscript. All data used in the paper are publicly available. Mathematica and Fortran codes are available on <https://zenodo.org> (see *Beuthe* [2020] in the reference list). This work is financially supported by the Belgian PRODEX program managed by the European Space Agency in collaboration with the Belgian Federal Science Policy Office.

Appendix A Elastic isostasy

This section lists a few key results of Paper I that are specific to elastic isostasy. Elastic isostatic ratios are invariant under a global rescaling of the shear modulus of the shell (μ -invariance) so that they can be computed in the fluid limit. Since deviatoric Love numbers tend to zero in this limit, isostatic ratios are controlled by the partial derivatives of Love numbers with respect to the shear modulus of the shell (L’Hôpital’s rule). In particular, the shape ratio given by Eq. (15) (with a superscript ‘e’ for ‘elastic’) becomes

$$S_n^e = \frac{\dot{h}_o^L + \zeta_n^\circ \dot{h}_o^I}{\dot{h}_s^L + \zeta_n^\circ \dot{h}_s^I}, \quad (\text{A.1})$$

where ζ_n° denotes the fluid limit of the loading ratio and

$$\dot{h}_j^J = \left. \frac{\partial}{\partial \mu_0} h_{je}^J \right|_{\mu_0=0}. \quad (\text{A.2})$$

If the shell has uniform elastic properties, μ_0 is simply the shear modulus of the material; if elasticity varies with depth, μ_0 is an arbitrary reference value in the factorization $\mu_s(r) =$

$\mu_0 f(r)$. If the shell is stratified into N homogeneous layers with shear moduli (μ_1, \dots, μ_N) , the partial derivative for the radial Love number can be expressed with the chain rule as

$$\begin{aligned} \dot{h}_j^J &= \sum_{i=1}^N \left(\frac{\partial}{\partial \mu_i} h_{je}^J \right) \left(\frac{\partial}{\partial \mu_0} \mu_i \right) \Big|_{\mu_0=0} \\ &= \sum_{i=1}^N f_i \frac{\partial}{\partial \mu_i} h_{je}^J \Big|_{\mu_1=0 \dots \mu_N=0}, \end{aligned} \quad (\text{A.3})$$

where f_i is the discretized version of $f(r)$. A similar expression holds for \dot{k}_j^J . Eq. (A.3) will be useful to prove the equivalence between zero deflection isostasy and ‘constant shape’ viscoelastic isostasy.

The fluid loading ratios for zero deflection isostasy (ZDI) and for minimum stress isostasy (MSI) are given by

$$\zeta_n^{\circ\text{ZDI}} = -\frac{\Delta\xi_1}{\xi_{s1}} \frac{x}{\alpha}, \quad (\text{A.4})$$

$$\zeta_n^{\circ\text{MSI}} = \frac{1}{x} \frac{\beta(1-a) + b}{\beta c + d}, \quad (\text{A.5})$$

where (a, b, c, d) are the same as in Eqs. (17)-(18) (the MSI formula is derived under the assumption of an incompressible body with a homogenous shell). The isostatic family parameters α and β reflect the choice of boundary conditions. For ZDI, $\alpha = 0$ (resp. $\alpha = \infty$) if the radial displacement (or deflection) is zero at the top (resp. bottom) of the shell. For MSI, $\beta = 0$ (resp. $\beta = -\infty$) if the shape of the top (resp. bottom) of the shell is held constant when the energy is minimized. MSI and ZDI isostatic ratios are equal if their loading ratios are equal, which occurs if

$$\alpha = -\frac{b}{c} \frac{\beta c + d}{\beta(1-a) + b}. \quad (\text{A.6})$$

This duality can be used to obtain MSI isostatic ratios from ZDI ones, which are more easily computable.

If the body is incompressible and has a homogeneous shell, Love numbers can be expressed as ratio of degree-2 polynomials in μ_s with generic coefficients as in Eq. (B.1). In that case, the ZDI shape ratio reads

$$S_n^{\text{ZDI}} = -\frac{\xi_{s1}}{x\Delta\xi_1} \frac{B_s^L + \alpha B_o^L}{B_s^I + \alpha B_o^I}. \quad (\text{A.7})$$

The coefficients B_j^J are given in analytical form in the complementary software for an incompressible body with homogeneous shell, ocean, and core. The topographic ratio takes a particularly simple form which is independent of the properties of the core:

$$T_n^{\text{ZDI}} = -\frac{\xi_{s1}}{\Delta\xi_1} \frac{1}{\gamma_o} \frac{\alpha P_n(x) + Q_n(x)}{\alpha Q_n'(x) + x^2 P_n(x)}, \quad (\text{A.8})$$

where the functions $(P_n(x), Q_n(x), Q'_n(x))$ are polynomials in x with coefficients defined in Table 4 of Paper I (see also complementary software). In Paper I, I conjectured that the topographic ratio is in general independent of the internal structure below the shell, in which case Eq. (A.8) is valid for bodies with stratified core and stratified ocean as long as the shell is homogeneous and incompressible. Using Eqs. (17)-(18), one can convert the topographic ratio into the shape ratio and compensation factor.

In the thin shell limit, the ZDI and MSI isostatic ratios do not depend on their respective isostatic family parameters α and β up to first order in $\varepsilon = 1 - x$. In particular, the shape ratio tends to

$$S_n^{\text{TSI}} \cong -\frac{\xi_{s1}}{\Delta\xi_1} \left(1 + \varepsilon \frac{n-1}{2n+1-3\xi_{o1}} \left(3\xi_{o1} - \frac{(2n+1)(n+2)}{2n^2+2n-1} \right) \right), \quad (\text{A.9})$$

where ‘TSI’ stands for Thin Shell Isostasy (the core is assumed to be infinitely rigid). Therefore the ZDI and MSI compensation factors do not depend on their isostatic family parameters to leading order in the thin shell limit. While the thin shell limit is not a good approximation for the compensation factor except at the longest wavelengths, the compensation factor is very well approximated by computing it from the shape ratio (Eq. (A.9)) with Eq. (18). This model of ‘improved’ thin shell isostasy is very close to elastic isostasy with local compensation (see Fig. 10 of Paper I).

Appendix B Constant loading of a homogeneous shell

B.1 Viscoelastic Love numbers

Consider an incompressible 3-layer body with a homogeneous shell (the ocean and the core are not necessarily homogeneous). The shell is viscoelastic, the ocean is inviscid, and the core is elastic (including the limits in which the core is either infinitely rigid or fluid-like). In that case, there are only two relaxation (buoyancy) modes associated with the shell boundaries (see Section 1.8 of *Sabadini et al.* [2016]). Two modes mean that the Love numbers have two poles in the Laplace domain. Thus, Laplace-domain Love numbers can be written as the ratio of two degree-2 polynomials in the s -dependent shear modulus $\tilde{\mu}$ (the dependence on s is implicit). The principle of correspondence tells us the same thing: Laplace-domain Love numbers are given by elastic Love numbers (Eqs. (D.1) and (D.12) of Paper I) in which the elastic shear modulus is replaced by the s -dependent shear modulus $\tilde{\mu}$. For example, viscoelastic radial Love numbers can be read from the generic form given by Eq. (D.1) of Paper I:

$$\tilde{h}_j^J(s) = \frac{A_j^J + B_j^J \tilde{\mu}(s) + C_j^J \tilde{\mu}(s)^2}{D + E \tilde{\mu}(s) + F \tilde{\mu}(s)^2}, \quad (\text{B.1})$$

The denominator coefficients are common to all Love numbers and determine the relaxation times. The numerator coefficients (A_j^J, B_j^J, C_j^J) satisfy Eqs. (D.2)-(D.5) of Paper I:

$$A_j^J = D h_j^{J_o}, \quad (\text{B.2})$$

$$C_j^J = 0, \quad (\text{B.3})$$

$$A_s^L B_o^I + A_o^I B_s^L = (E/D) A_s^L A_o^I, \quad (\text{B.4})$$

$$B_s^L B_o^I - B_o^L B_s^I = (F/D) A_s^L A_o^I. \quad (\text{B.5})$$

The first two constraints come from the limits in which the shell tends to be fluid-like or infinitely rigid. The last two come from the assumption of μ -invariance of zero-deflection elastic isostasy (they were checked analytically for a model with three homogeneous layers).

B.2 Poles and decay times

The two (negative) $\tilde{\mu}$ -poles of Eq. (B.1) are given by

$$\mu_{\pm} = \frac{1}{2F} \left(-E \pm \sqrt{E^2 - 4DF} \right), \quad (\text{B.6})$$

and satisfy the identities

$$\mu_+ \mu_- = D/F \quad \text{and} \quad \mu_+ + \mu_- = -E/F. \quad (\text{B.7})$$

For Maxwell rheology (Eq. (21)), the corresponding (negative) s -poles are given by

$$\mu_{\pm} = \frac{\mu_e s_{\pm}}{s_{\pm} + \mu_e/\eta} \Leftrightarrow s_{\pm} = -\frac{\mu_e}{\eta} \frac{\mu_{\pm}}{\mu_{\pm} - \mu_e}. \quad (\text{B.8})$$

The viscoelastic decay times are given by

$$\tau_{\pm} = -1/s_{\pm}, \quad (\text{B.9})$$

with the longest time scale corresponding to s_+ , the pole closest to zero. Viscoelastic decay times reduce to viscous decay times (Eq. (54)) in the limit of infinite elastic modulus:

$$\tau_{\pm}^{\text{viscous}} = -\eta/\mu_{\pm}. \quad (\text{B.10})$$

This property can be proven by showing that the viscous decay times are the solutions of the following equation (obtained from $D + E\mu_{\pm} + F\mu_{\pm}^2 = 0$):

$$D(-\tau_{\pm}^{\text{viscous}}/\eta)^2 + E(-\tau_{\pm}^{\text{viscous}}/\eta) + F = 0. \quad (\text{B.11})$$

B.3 Residues

The residues associated with the poles s_{\pm} are given by

$$r_{j\pm}^J = \left(\frac{\mu_e s_{\pm}}{\mu_{\pm}} \right)^2 \frac{1}{s_{\pm} - s_{\mp}} \frac{A_j^J + B_j^J \mu_{\pm} + C_j^J \mu_{\pm}^2}{D + E\mu_e + F\mu_e^2}. \quad (\text{B.12})$$

All factors except the numerator of the last term are the same whatever the Love number. These common factors cancel when computing the ratio of residues as required for the shape ratio and compensation factor (Eqs. (35)-(36)). The shape ratio can be computed either with top loading or from bottom loading:

$$S_n^{\text{VeLI,top}} = \frac{r_{o+}^L}{r_{s+}^L} = \frac{B_o^L \mu_+}{A_s^L + B_s^L \mu_+}, \quad (\text{B.13})$$

$$S_n^{\text{VeLI,bot}} = \frac{r_{o+}^I}{r_{s+}^I} = \frac{A_o^I + B_o^I \mu_+}{B_s^I \mu_+}. \quad (\text{B.14})$$

These ratios do not depend on μ_e or η . Moreover, the two ratios are identical if

$$A_s^L A_o^I + (A_s^L B_o^I + A_o^I B_s^L) \mu_+ + (B_s^L B_o^I - B_o^L B_s^I) \mu_+^2 = 0, \quad (\text{B.15})$$

which is true because this equation is proportional to $D + E\mu_+ + F\mu_+^2 = 0$ thanks to the identities (B.4)-(B.5). Therefore, μ -invariance implies that viscoelastic isostasy with constant load does not depend of the loading ratio.

For further analysis, the shape ratio is set into equivalent expressions where μ_+ appears either only in the denominator or only in the numerator:

$$S_n^{\text{VeLI}} = \frac{\xi_{sn} B_o^L}{F\mu_+ - x\Delta\xi_n B_o^I} \quad (\text{B.16})$$

$$= \frac{F\mu_+ - \xi_{sn} B_s^L}{x\Delta\xi_n B_s^I}. \quad (\text{B.17})$$

These formulas were obtained by multiplying Eqs. (B.13)-(B.14) by μ_-/μ_+ and using Eqs. (B.2), (B.4), and (B.7).

B.4 Thin shell limit

Recall that the thin shell expansion parameter is $\varepsilon = 1 - x = d/R$. In Paper I, I showed that the coefficients D and F decrease faster with shell thickness than E , whereas B_j^J decreases as fast as E . Given that $B_j^J/E \rightarrow -1/\xi_{on}$ in the thin shell limit (Eq. (D.21) of Paper I), the four coefficients B_j^J start to differ at $\mathcal{O}(\varepsilon^2)$. Suppose that E is $\mathcal{O}(\varepsilon)$, as is the case in my explicit computation (all coefficients can of course be multiplied by the

same power of $1 - x = \varepsilon$); then B_j^J is $\mathcal{O}(\varepsilon)$ whereas D and F are $\mathcal{O}(\varepsilon^2)$. Thus, the μ -poles (Eq. (B.6)) can be approximated to leading order in ε by

$$(\mu_+, \mu_-) \cong - \left(\frac{D}{E}, \frac{E}{F} \right). \quad (\text{B.18})$$

If the ocean is homogeneous and the core is infinitely rigid, the expansions of D/E and E/F to order ε are given by (in nondimensional form)

$$\bar{\mu}_+ \cong - \frac{n(n+1)}{2(2n^2+2n-1)} \frac{\xi_{s1}}{\xi_{o1}} \Delta\xi_1 \varepsilon + \mathcal{O}(\varepsilon^2), \quad (\text{B.19})$$

$$\bar{\mu}_- \cong - \frac{2n^2+2n-1}{6(n-1)(n+2)} \xi_{o1} (1 - \xi_{on}) \frac{1}{\varepsilon} + \mathcal{O}(1), \quad (\text{B.20})$$

where $\bar{\mu}_\pm = \mu_\pm / \mu_G$, μ_G being the gravitational rigidity $\mu_G = \rho_s g_s R_s$. Eq. (B.19), but not Eq. (B.20), remains correct if the core is homogeneous and elastic.

Thus $|\bar{\mu}_+| \ll 1$ if the shell is thin. For large satellites, μ_e has a magnitude comparable to μ_G , whereas $\mu_e \gg \mu_G$ for small satellites. Therefore $|\mu_+| \ll \mu_e$ for physically plausible values of μ_e . Because of this, the s -pole closest to zero (Eq. (B.8)) can be approximated by

$$s_+ \cong \frac{\mu_+}{\eta}. \quad (\text{B.21})$$

This value is independent of μ_e and is inversely proportional to the longest viscous decay time (Eq. (B.10)).

The thin shell limit of the shape ratio is most conveniently obtained from Eqs. (B.16)-(B.17) given that $F\mu_+ \sim \mathcal{O}(\varepsilon^3)$ can be dropped from the equation:

$$S_n^{\text{VeLI}} \cong - \frac{\xi_{s1}}{x\Delta\xi_1} \frac{B_o^L}{B_o^I} + \mathcal{O}(\varepsilon^2) \quad (\text{B.22})$$

$$\cong - \frac{\xi_{s1}}{x\Delta\xi_1} \frac{B_s^L}{B_s^I} + \mathcal{O}(\varepsilon^2). \quad (\text{B.23})$$

These expressions coincide with the ZDI shape ratio in which either $\alpha = 0$ or $\alpha = \infty$ (Eq. (A.7)). Thus, the expansion to $\mathcal{O}(\varepsilon)$ of the viscoelastic ‘constant load’ shape ratio must agree with the expansion to $\mathcal{O}(\varepsilon)$ of the elastic shape ratio. The explicit thin shell limit of the shape ratio is given by Eq. (A.9) under the assumption of an infinitely rigid core.

B.5 Shape ratio at high harmonic degree

At high harmonic degree, the viscoelastic shape ratio for a homogeneous shell depends on the harmonic degree n , on the relative radius of shell-ocean boundary x , and on the parameter ψ defined by

$$\psi = \gamma_o x \frac{\Delta\xi_1}{\xi_{s1}}, \quad (\text{B.24})$$

with $\psi \leq 1$ being the physically most likely case. The asymptotic behaviour of the ‘constant load’ viscoelastic shape ratio at high harmonic degree is given by

$$S_n^{\text{VeLI}} \sim -\frac{1}{n x^n} \frac{1}{1-x^2} \left(\frac{1}{\psi} - 1 \right) \quad \text{if } \psi \leq 1, \quad (\text{B.25})$$

$$S_n^{\text{VeLI}} \sim -n x^n \frac{1-x^2}{x} \frac{1}{\psi-1} \quad \text{if } \psi > 1. \quad (\text{B.26})$$

The formulas for $\psi \leq 1$ and $\psi > 1$ were obtained by substituting the expressions of Table 5 into Eq. (B.14) and Eq. (B.13), respectively (doing the other way around is tricky because dominant terms cancel at the leading asymptotic order).

The asymptotic behaviour of the ‘constant shape’ viscoelastic shape ratio at high harmonic degree is given by

$$S_n^{\text{VeSI,top}} \sim -n x^n \frac{1-x^2}{x} \frac{1}{\psi}, \quad (\text{B.27})$$

$$S_n^{\text{VeSI,bot}} \sim -\frac{1}{n x^n} \frac{1}{1-x^2} \frac{1}{\psi}. \quad (\text{B.28})$$

These formulas were obtained by substituting the expressions of Table 5 into Eq. (46) with either $\zeta_n^V = 0$ (top load) or $\zeta_n^V = \pm\infty$ (bottom load).

Thus, S_n^{VeLI} tends either to a constant multiple of $S_n^{\text{VeSI,bot}}$ or of $S_n^{\text{VeSI,top}}$, depending on the value of ψ :

$$S_n^{\text{VeLI}} \sim (1-\psi) S_n^{\text{VeSI,bot}} \quad \text{if } \psi \leq 1, \quad (\text{B.29})$$

$$S_n^{\text{VeLI}} \sim \frac{\psi}{\psi-1} S_n^{\text{VeSI,top}} \quad \text{if } \psi > 1. \quad (\text{B.30})$$

Appendix C Slow viscous flow

C.1 Differential equations

Slow viscous flow is described by 6 variables with the dimension of velocity, which can be grouped into two sets [Hager and Clayton, 1989]. The first set, mainly characterized by velocity and stress, reads $\mathbf{u} = (u_1, u_2, u_3, u_4)^T$, where u_1 and u_2 are the radial and tangential velocities, $u_3 = r y_3 / \eta_0 + (\rho / \eta_0) r y_5$ is related to the (Eulerian) radial stress y_3 and the gravitational potential y_5 , and $u_4 = r y_4 / \eta_0$ is the potential for the (Eulerian) radial-tangential stress. The second set, including only gravity variables, reads $\mathbf{v} = (v_1, v_2)^T$ where $v_1 = (\rho_0 / \eta_0) r y_5$ and $v_2 = (\rho_0 / \eta_0) r^2 y_6$ are associated with the gravity potential and its derivative, respectively. A reference density ρ_0 and a reference viscosity η_0 have been

Table 5: High-degree asymptotic behaviour of Love number generic coefficients and μ -pole closest to zero for a 3-layer incompressible body with homogeneous layers (the core can be rigid, fluid, or elastic). The parameter ψ is defined by Eq. (B.24) while fluid Love numbers $h_j^{J^\circ}$ are given in Table 2.

Coeff.	Asymptotic behaviour
D/F	$(\xi_{s1})^2 \psi / (4n^2)$
E/F	$\xi_{s1} (1 + \psi) / (2n)$
A_j^J / F	$h_j^{J^\circ} D / F$
B_s^L / F	$-1/3$
B_o^L / F	$-n x^{n-1} (1 - x^2) / 3$
B_s^I / F	$-n x^n (1 - x^2) \gamma_o / 3$
B_o^I / F	$-\gamma_o / 3$
μ_+	$-\xi_{s1} (1 + \psi - 1 - \psi) / (4n)$
$\mu_+(\psi \leq 1)$	$-\xi_{s1} \psi / (2n)$
$\mu_+(\psi \geq 1)$	$-\xi_{s1} / (2n)$

introduced for normalization purposes, but the solution should not depend on them. In a homogeneous layer, the 6 variables satisfy

$$r \frac{d\mathbf{u}}{dr} = \mathbf{A} \cdot \mathbf{u}, \quad (\text{C.1})$$

$$r \frac{d\mathbf{v}}{dr} = \mathbf{B} \cdot \mathbf{v}, \quad (\text{C.2})$$

where

$$\mathbf{A} = \begin{pmatrix} -2 & -\delta_n & 0 & 0 \\ -1 & 1 & 0 & 1/\eta^* \\ 12\eta^* & 6\eta^* \delta_n & 1 & -\delta_n \\ -6\eta^* & -2\eta^* (2\delta_n + 1) & -1 & -2 \end{pmatrix}, \quad (\text{C.3})$$

$$\mathbf{B} = \begin{pmatrix} 1 & 1 \\ -\delta_n & 0 \end{pmatrix}, \quad (\text{C.4})$$

in which $\eta^* = \eta/\eta_0$ and $\delta_n = -n(n+1)$ as elsewhere.

C.2 Fundamental matrices

The systems of differential equations (C.1) and (C.2) can be solved with the (*Eulerian*) *propagator matrix method*, in which the propagator matrix relates the variables at two

different radii within the layer. *Hager and Clayton* [1989] compute the propagator matrices with Sylvester's formula, but without giving the result for \mathbf{A} (because it is too long), while there are typos in their propagator matrix for \mathbf{B} . Instead of computing directly the propagator matrix, I will first solve the equations in terms of free constants. In this way, I can express more compactly the propagator in terms of the *fundamental matrix*, as is commonly done in gravitational-elastic theory. If $\mathbf{u} \sim r^p$ and $\mathbf{v} \sim r^q$, then Eqs. (C.1)-(C.2) are transformed into eigenvalue problems:

$$p \mathbf{u} = \mathbf{A} \cdot \mathbf{u}, \quad (\text{C.5})$$

$$q \mathbf{v} = \mathbf{B} \cdot \mathbf{v}. \quad (\text{C.6})$$

The eigenvalues of \mathbf{A} and \mathbf{B} are $(n+1, n-1, -n, -(n+2))$ and $(n+1, -n)$, respectively. The solutions can be written as a linear combination of the eigenvectors multiplied by the corresponding r^p or r^q or, in matrix form:

$$\mathbf{u}(r) = \mathbf{Y}_A(r) \cdot \mathbf{c}_u, \quad (\text{C.7})$$

$$\mathbf{v}(r) = \mathbf{Y}_B(r) \cdot \mathbf{c}_v, \quad (\text{C.8})$$

where \mathbf{c}_u and \mathbf{c}_v are vectors of 4 free constants and 2 free constants, respectively. The fundamental matrices are given by

$$\mathbf{Y}_A(r) = \mathbf{C}_A \cdot \bar{\mathbf{Y}}_A \cdot \mathbf{D}_A(r), \quad (\text{C.9})$$

$$\mathbf{Y}_B(r) = \bar{\mathbf{Y}}_B \cdot \mathbf{D}_B(r), \quad (\text{C.10})$$

where

$$\bar{\mathbf{Y}}_A = \begin{pmatrix} 1 & 1 & 1 & 1 \\ \frac{n+3}{n(n+1)} & \frac{1}{n} & -\frac{n-2}{n(n+1)} & -\frac{1}{n+1} \\ \frac{n^2-n-3}{n} & n-1 & -\frac{n^2+3n-1}{n+1} & -(n+2) \\ \frac{n+2}{n+1} & \frac{n-1}{n} & \frac{n-1}{n} & \frac{n+2}{n+1} \end{pmatrix}, \quad (\text{C.11})$$

$$\bar{\mathbf{Y}}_B = \begin{pmatrix} 1 & 1 \\ n & -(n+1) \end{pmatrix}, \quad (\text{C.12})$$

while \mathbf{C}_A , $\mathbf{D}_A(r)$, and $\mathbf{D}_B(r)$ are diagonal matrices with elements

$$\text{diag}(\mathbf{C}_A) = (1, 1, 2\eta^*, 2\eta^*), \quad (\text{C.13})$$

$$\text{diag}(\mathbf{D}_A(r)) = (\bar{r}^{n+1}, \bar{r}^{n-1}, \bar{r}^{-n}, \bar{r}^{-n-2}), \quad (\text{C.14})$$

$$\text{diag}(\mathbf{D}_B(r)) = (\bar{r}^{n+1}, \bar{r}^{-n}), \quad (\text{C.15})$$

where $\bar{r} = r/r_0$ (r_0 is an arbitrary reference radius introduced so that the fundamental matrix is nondimensional). The solution for \mathbf{u} is similar to Eq. (22) of *Ricard et al.* [1984], but without the typos in the 3rd term of u_2 and in the 3rd and 4th terms of u_3 (note

that the solution without self-gravity of *Ricard et al.* [1984] is formally equivalent to the solution \mathbf{u} of *Hager and Clayton* [1989] because of gravity decoupling in the latter paper).

The inverse fundamental matrices read

$$\mathbf{Y}_A^{-1}(r) = \mathbf{D}_A^{-1}(r) \cdot \bar{\mathbf{Y}}_A^{-1} \cdot \mathbf{C}_A^{-1}, \quad (\text{C.16})$$

$$\mathbf{Y}_B^{-1}(r) = \mathbf{D}_B^{-1}(r) \cdot \bar{\mathbf{Y}}_B^{-1}, \quad (\text{C.17})$$

where

$$\bar{\mathbf{Y}}_A^{-1} = \mathbf{E}_A \cdot \begin{pmatrix} -(n+2) & n(n+2) & -1 & n \\ \frac{n^2+3n-1}{n+1} & -(n^2-1) & 1 & -(n-2) \\ n-1 & n^2-1 & -1 & -(n+1) \\ -\frac{n^2-n-3}{n} & -n(n+2) & 1 & n+3 \end{pmatrix}, \quad (\text{C.18})$$

$$\bar{\mathbf{Y}}_B^{-1} = \frac{1}{2n+1} \begin{pmatrix} n+1 & 1 \\ n & -1 \end{pmatrix}, \quad (\text{C.19})$$

in which \mathbf{E}_A is a diagonal matrix with elements

$$\text{diag}(\mathbf{E}_A) = \frac{n(n+1)}{2n+1} \left(\frac{1}{2n+3}, \frac{1}{2n-1}, \frac{1}{2n-1}, \frac{1}{2n+3} \right). \quad (\text{C.20})$$

C.3 Propagator matrices

Using Eqs. (C.7)-(C.8) twice and eliminating the free constants, I can relate the variables at radius R_s to those at radius R_o ,

$$\mathbf{u}(R_s) = \mathbf{P}_A(R_s/R_o) \cdot \mathbf{u}(R_o), \quad (\text{C.21})$$

$$\mathbf{v}(R_s) = \mathbf{P}_B(R_s/R_o) \cdot \mathbf{v}(R_o), \quad (\text{C.22})$$

where \mathbf{P}_A and \mathbf{P}_B are the propagator matrices:

$$\mathbf{P}_A(R_s/R_o) = \mathbf{Y}_A(R_s) \cdot \mathbf{Y}_A^{-1}(R_o), \quad (\text{C.23})$$

$$\mathbf{P}_B(R_s/R_o) = \mathbf{Y}_B(R_s) \cdot \mathbf{Y}_B^{-1}(R_o). \quad (\text{C.24})$$

For example, the propagator matrix for \mathbf{B} is given by

$$\mathbf{P}_B(R_s/R_o) = \frac{1}{2n+1} \begin{pmatrix} (n+1)x^{-n-1} + nx^n & x^{-n-1} - x^n \\ n(n+1)(x^{-n-1} - x^n) & nx^{-n-1} + (n+1)x^n \end{pmatrix}, \quad (\text{C.25})$$

where $x = R_o/R_s$. This formula corrects typos in Eq. (4.44) of *Hager and Clayton* [1989]. It is straightforward to compute \mathbf{P}_A as the two-point product of the fundamental matrix and its inverse, but the result is quite long and will not be given here.

C.4 Boundary conditions

The boundary conditions for the radial-tangential stress variable u_4 are very simple (free-slip):

$$u_4(R_o) = u_4(R_s) = 0. \quad (\text{C.26})$$

The variable u_3 is a combination of the radial stress and the gravity potential. The bottom boundary condition for u_3 does not appear explicitly in *Hager and Clayton* [1989] (see their Eq. (4.53)), while the surface boundary condition contains typos (see after their Eq. (4.54)). Here are the appropriate boundary conditions:

$$u_3(R_s) = -\rho_s (g_s R_s \delta r_s / \eta_0 - v_1(R_s) / \rho_0), \quad (\text{C.27})$$

$$u_3(R_o) = (\rho_o - \rho_s) (g_o R_o \delta r_o / \eta_0 - v_1(R_o) / \rho_0), \quad (\text{C.28})$$

where δr_j is the displacement of interface R_j . The boundary conditions for the derivative of the gravity potential at harmonic degree n are given by Eqs. (4.56) and (4.58) of *Hager and Clayton* [1989]:

$$v_2(R_s) = -(n+1) v_1(R_o) + 4\pi G R_s^2 \rho_s (\rho_0 / \eta_0) \delta r_s, \quad (\text{C.29})$$

$$v_2(R_o) = n v_1(R_o) - 4\pi G R_o^2 (\rho_o - \rho_s) (\rho_0 / \eta_0) \delta r_o. \quad (\text{C.30})$$

Solving Eq. (C.22) for v_1 with the appropriate boundary conditions for v_2 (Eqs. (C.29)-(C.30)) and using nondimensional parameters, I get boundary conditions for the gravity potential variable in terms of boundary displacements:

$$v_1(R_s) = \xi_{sn} (\delta r_s / \tau_0) + \Delta \xi_n x^{n+2} (\delta r_o / \tau_0), \quad (\text{C.31})$$

$$v_1(R_o) = \xi_{sn} x^{n+1} (\delta r_s / \tau_0) + \Delta \xi_n x^2 (\delta r_o / \tau_0), \quad (\text{C.32})$$

where $\tau_0 = \eta_0 / (\rho_0 g_s R_s)$ is a reference time. These results are equivalent to Eqs. (C.1)-(C.2) of Paper I, giving the gravitational perturbations in terms of the shapes of the shell boundaries (noting that $H_{cn} = 0$ because the core is rigid, and that the definition of v_1 introduces an additional factor of x).

Substituting Eqs. (C.31)-(C.32) into Eqs. (C.27)-(C.28) and using nondimensional parameters, I get boundary conditions for stress variables in terms of boundary displacements:

$$u_3(R_s) = \xi_{s1} ((\xi_{sn} - 1) (\delta r_s / \tau_0) + \Delta \xi_n x^{n+2} (\delta r_o / \tau_0)), \quad (\text{C.33})$$

$$u_3(R_o) = \Delta \xi_1 (-\xi_{sn} x^{n+1} (\delta r_s / \tau_0) + x (\gamma_o - \Delta \xi_n x) (\delta r_o / \tau_0)), \quad (\text{C.34})$$

where the reference density ρ_0 is set equal to the bulk density ρ_b so that

$$\tau_0 = \eta_0 / (\rho_b g_s R_s). \quad (\text{C.35})$$

C.5 Reduced propagation system

Following *Ermakov et al.* [2017], I start by solving the propagation equation for the gravity variables for a shell of uniform density,

$$\begin{pmatrix} v_1(R_s) \\ v_2(R_s) \end{pmatrix} = \mathbf{P}_B \cdot \begin{pmatrix} v_1(R_o) \\ v_2(R_o) \end{pmatrix}, \quad (\text{C.36})$$

where \mathbf{P}_B is the matrix given by Eq. (C.25). In this way, the gravity potential can be expressed in terms of boundary displacements, making it possible to express the boundary conditions on the radial stress variable u_3 in terms of boundary displacements (Eqs. (C.31)-(C.34)). The boundary conditions on the tangential-radial stress variable u_4 are free-slip (Eq. (C.26)). The propagation of the velocity variables (u_1, u_2) and stress variables (u_3, u_4) from the bottom of the shell to the surface reads

$$\begin{pmatrix} u_1(R_s) \\ \dots \\ u_4(R_s) \end{pmatrix} = \mathbf{P}_A \cdot \begin{pmatrix} u_1(R_o) \\ \dots \\ u_4(R_o) \end{pmatrix}, \quad (\text{C.37})$$

where \mathbf{P}_A is the two-point matrix product defined by Eq. (C.23). For our isostatic problem, this 4×4 matrix system can be reduced to two equations:

1. Drop the equation for the surface tangential velocity $u_2(R_s)$ from the system because isostatic ratios depend only on radial displacements and velocities.
2. Substitute the boundary conditions for u_3 and u_4 into the propagation system.
3. Eliminate the bottom tangential velocity $u_2(R_o)$ from the propagation system by using the equation for $u_4(R_s)$.

This procedure yields two equations (or reduced propagation system) for the radial velocities ($u_1(R_s), u_1(R_o)$) and the radial displacements ($\delta r_s, \delta r_o$).

References

- A, G., J. Wahr, and S. Zhong (2013), Computations of the viscoelastic response of a 3-D compressible Earth to surface loading: an application to Glacial Isostatic Adjustment in Antarctica and Canada, *Geophys. J. Int.*, *192*(2), 557–572, doi:10.1093/gji/ggs030.
- Beuthe, M. (2018), Enceladus’s crust as a non-uniform thin shell: I tidal deformations, *Icarus*, *302*, 145–174, doi:10.1016/j.icarus.2017.11.009.
- Beuthe, M. (2019), Enceladus’s crust as a non-uniform thin shell: II tidal dissipation, *Icarus*, *332*, 66–91, doi:10.1016/j.icarus.2019.05.035.
- Beuthe, M. (2020), IsostasyWithLove: Mathematica and Fortran codes for analytical isostasy in 3-layer bodies, *Zenodo*, doi:10.5281/zenodo.4297495.
- Beuthe, M. (2021), Isostasy with Love: I Elastic equilibrium, *Geophys. J. Int.*, *225*, 2157–2193, doi:10.1093/gji/ggab073.
- Beuthe, M., A. Rivoldini, and A. Trinh (2016), Enceladus’s and Dione’s floating ice shells supported by minimum stress isostasy, *Geophys. Res. Lett.*, *43*, 10,088–10,096, doi:10.1002/2016GL070650.
- Bird, P. (1991), Lateral extrusion of lower crust from under high topography in the isostatic limit, *J. Geophys. Res.*, *96*(B6), 10,275–10,286, doi:10.1029/91JB00370.
- Bland, M. T., K. N. Singer, W. B. McKinnon, and P. M. Schenk (2012), Enceladus’ extreme heat flux as revealed by its relaxed craters, *Geophys. Res. Lett.*, *39*(17), L17204, doi:10.1029/2012GL052736.
- Bland, M. T., C. A. Raymond, P. M. Schenk, R. R. Fu, T. Kneissl, J. H. Pasckert, H. Hiesinger, F. Preusker, R. S. Park, S. Marchi, S. D. King, J. C. Castillo-Rogez, and C. T. Russell (2016), Composition and structure of the shallow subsurface of Ceres revealed by crater morphology, *Nat. Geosci.*, *9*(7), 538–542, doi:10.1038/ngeo2743.
- Bland, M. T., K. N. Singer, W. B. McKinnon, and P. M. Schenk (2017), Viscous relaxation of Ganymede’s impact craters: Constraints on heat flux, *Icarus*, *296*, 275–288, doi:10.1016/j.icarus.2017.06.012.
- Cadek, O., M. Behoukova, G. Tobie, and G. Choblet (2017), Viscoelastic relaxation of Enceladus’s ice shell, *Icarus*, *291*, 31–35, doi:10.1016/j.icarus.2017.03.011.
- Cadek, O., O. Soucek, and M. Behoukova (2019a), Is Airy isostasy applicable to icy moons?, *Geophys. Res. Lett.*, *46*(24), 14,299–14,306, doi:10.1029/2019GL085903.
- Cadek, O., O. Soucek, M. Behoukova, G. Choblet, G. Tobie, and J. Hron (2019b), Long-term stability of Enceladus’ uneven ice shell, *Icarus*, *319*, 476–484, doi:10.1016/j.icarus.2018.10.003.
- Cambiotti, G., V. Klemann, and R. Sabadini (2013), Compressible viscoelastodynamics of a spherical body at long timescales and its isostatic equilibrium, *Geophys. J. Int.*, *193*(3), 1071–1082, doi:10.1093/gji/ggt026.
- Dahlen, F. A. (1982), Isostatic geoid anomalies on a sphere, *J. Geophys. Res.*, *87*, 3943–3947, doi:10.1029/JB087iB05p03943.
- Davies, D. R., A. P. Valentine, S. C. Kramer, N. Rawlinson, M. J. Hoggard, C. M. Eakin, and C. R. Wilson (2019), Earth’s multi-scale topographic response to global mantle flow, *Nat. Geosci.*, *12*(10), 845–850, doi:10.1038/s41561-019-0441-4.
- Dombard, A. J., and W. B. McKinnon (2000), Long-term retention of impact crater topography on Ganymede, *Geophys. Res. Lett.*, *27*(22), 3663–3666, doi:10.1029/2000GL011695.
- Dombard, A. J., and W. B. McKinnon (2006), Elastoviscoplastic relaxation of impact crater topography with application to Ganymede and Callisto, *J. Geophys. Res.*, *111*(E1), E01001, doi:10.1029/2005JE002445.
- Durante, D., D. J. Hemingway, P. Racioppa, L. Iess, and D. J. Stevenson (2019), Titan’s gravity field and interior structure after Cassini, *Icarus*, *326*, 123–132, doi:10.1016/j.icarus.2019.03.003.

- Durham, W. B., and L. A. Stern (2001), Rheological properties of water ice - Applications to satellites of the outer planets, *Ann. Rev. Earth Planet. Sci.*, *29*, 295–330, doi:10.1146/annurev.earth.29.1.295.
- Dyke, P. (2014), *An Introduction to Laplace Transforms and Fourier Series*, Springer-Verlag, London, doi:10.1007/978-1-4471-6395-4.
- Ermakov, A. I., R. R. Fu, J. C. Castillo-Rogez, C. A. Raymond, R. S. Park, F. Preusker, C. T. Russell, D. E. Smith, and M. T. Zuber (2017), Constraints on Ceres' internal structure and evolution from its shape and gravity measured by the Dawn spacecraft, *J. Geophys. Res.*, *122*, 2267–2293, doi:10.1002/2017JE005302.
- Fischer, H. J., and T. Spohn (1990), Thermal-orbital histories of viscoelastic models of Io (J1), *Icarus*, *83*(1), 39–65, doi:10.1016/0019-1035(90)90005-T.
- Flament, N. (2019), The deep roots of Earth's surface, *Nat. Geosci.*, *12*(10), 787–788, doi:10.1038/s41561-019-0447-y.
- Fowler, C. M. R. (2005), *The Solid Earth*, second ed., 728 pp., Cambridge University Press, Cambridge.
- Fu, R. R., B. H. Hager, A. I. Ermakov, and M. T. Zuber (2014), Efficient early global relaxation of asteroid Vesta, *Icarus*, *240*, 133–145, doi:10.1016/j.icarus.2014.01.023.
- Fu, R. R., A. I. Ermakov, S. Marchi, J. C. Castillo-Rogez, C. A. Raymond, B. H. Hager, M. T. Zuber, S. D. King, M. T. Bland, M. Cristina De Sanctis, F. Preusker, R. S. Park, and C. T. Russell (2017), The interior structure of Ceres as revealed by surface topography, *Earth Planet. Sci. Lett.*, *476*, 153–164, doi:10.1016/j.epsl.2017.07.053.
- Fuller, J., J. Luan, and E. Quataert (2016), Resonance locking as the source of rapid tidal migration in the Jupiter and Saturn moon systems, *Mon. Not. R. Astron. Soc.*, *458*(4), 3867–3879, doi:10.1093/mnras/stw609.
- Goldsby, D. L., and D. L. Kohlstedt (2001), Superplastic deformation of ice: Experimental observations, *J. Geophys. Res.*, *106*, 11,017–11,030, doi:10.1029/2000JB900336.
- Gratton, J. (1989), Crustal shortening, root spreading, isostasy, and the growth of orogenic belts: A dimensional analysis, *J. Geophys. Res.*, *94*(B11), 15,627–15,634, doi:10.1029/JB094iB11p15627.
- Grimm, R. E., and S. C. Solomon (1988), Viscous relaxation of impact crater relief on Venus: constraints on crustal thickness and thermal gradient., *J. Geophys. Res.*, *93*, 11,911–11,929, doi:10.1029/JB093iB10p11911.
- Hager, B. H., and R. W. Clayton (1989), Constraints on the structure of mantle convection using seismic observations, flow models, and the geoid, in *Mantle Convection*, edited by W. R. Peltier, pp. 657–763, New York: Gordon and Breach.
- Hager, B. H., and R. J. O'Connell (1978), Subduction zone dip angles and flow driven by plate motion, *Tectonophysics*, *50*(2), 111–133, doi:10.1016/0040-1951(78)90130-0.
- Hager, B. H., and R. J. O'Connell (1979), Kinematic models of large-scale flow in the Earth's mantle, *J. Geophys. Res.*, *84*(B3), 1031–1048, doi:10.1029/JB084iB03p01031.
- Hager, B. H., R. W. Clayton, M. A. Richards, R. P. Comer, and A. M. Dziewonski (1985a), Lower mantle heterogeneity, dynamic topography and the geoid, *Nature*, *313*(6003), 541–545, doi:10.1038/313541a0.
- Hager, B. H., R. W. Clayton, M. A. Richards, R. P. Comer, and A. M. Dziewonski (1985b), Erratum: Lower mantle heterogeneity, dynamic topography and the geoid, *Nature*, *314*(6013), 752, doi:10.1038/314752a0.
- Han, D., and J. Wahr (1995), The viscoelastic relaxation of a realistically stratified earth, and a further analysis of postglacial rebound, *Geophys. J. Int.*, *120*(2), 287–311, doi:10.1111/j.1365-246X.1995.tb01819.x.
- Hemingway, D., L. Iess, R. Tajeddine, and G. Tobie (2018), The interior of Enceladus, in *Enceladus and the Icy Moons of Saturn*, edited by P. M. Schenk, R. N. Clark, C. J. A. Howett, A. J. Verbiscer, and J. Hunter Waite, pp. 57–77, University of Arizona Press, Tucson, doi:10.2458/azu_uapress.9780816537075-ch004.
- Hemingway, D. J., and I. Matsuyama (2017), Isostatic equilibrium in spherical coordinates and implications for crustal thickness on the Moon, Mars, Enceladus, and elsewhere, *Geophys. Res. Lett.*, *44*(15), 7695–7705, doi:10.1002/2017GL073334.

- Hoggard, M. J., N. White, and D. Al-Attar (2016), Global dynamic topography observations reveal limited influence of large-scale mantle flow, *Nat. Geosci.*, *9*(6), 456–463, doi:10.1038/ngeo2709.
- Hussmann, H., and T. Spohn (2004), Thermal-orbital evolution of Io and Europa, *Icarus*, *171*, 391–410, doi:10.1016/j.icarus.2004.05.020.
- Iess, L., D. J. Stevenson, M. Parisi, D. Hemingway, R. A. Jacobson, J. I. Lunine, F. Nimmo, J. W. Armstrong, S. W. Asmar, M. Ducci, and P. Tortora (2014), The gravity field and interior structure of Enceladus, *Science*, *344*, 78–80, doi:10.1126/science.1250551.
- Jara-Oru e, H. M., and B. L. A. Vermeersen (2011), Effects of low-viscous layers and a non-zero obliquity on surface stresses induced by diurnal tides and non-synchronous rotation: The case of Europa, *Icarus*, *215*, 417–438, doi:10.1016/j.icarus.2011.05.034.
- Jeffreys, H. (1932), On the stresses in the Earth’s crust required to support surface inequalities. (Second paper.), *Geophys. Suppl. MNRAS*, *3*, 60–69, doi:10.1111/j.1365-246X.1932.tb00400.x.
- Jeffreys, H. (1943), The stress-differences in the Earth’s shell, *Geophys. Suppl. MNRAS*, *5*, 71–89, doi:10.1111/j.1365-246X.1943.tb00344.x.
- Jeffreys, H. (1959), *The Earth, 4th Ed.*, Cambridge University Press, Cambridge.
- Kamata, S., and F. Nimmo (2017), Interior thermal state of Enceladus inferred from the viscoelastic state of the ice shell, *Icarus*, *284*, 387–393, doi:10.1016/j.icarus.2016.11.034.
- Kamata, S., S. Sugita, and Y. Abe (2012), A new spectral calculation scheme for long-term deformation of Maxwellian planetary bodies, *J. Geophys. Res.*, *117*(E2), E02004, doi:10.1029/2011JE003945.
- Kamata, S., S. Sugita, Y. Abe, Y. Ishihara, Y. Harada, T. Morota, N. Namiki, T. Iwata, H. Hanada, H. Araki, K. Matsumoto, and E. Tajika (2013), Viscoelastic deformation of lunar impact basins: Implications for heterogeneity in the deep crustal paleo-thermal state and radioactive element concentration, *J. Geophys. Res.*, *118*(3), 398–415, doi:10.1002/jgre.20056.
- Kopp, R. E., F. J. Simons, J. X. Mitrovica, A. C. Maloof, and M. Oppenheimer (2009), Probabilistic assessment of sea level during the last interglacial stage, *Nature*, *462*(7275), 863–867, doi:10.1038/nature08686.
- Kvorka, J., O.  adek, G. Tobie, and G. Choblet (2018), Does Titan’s long-wavelength topography contain information about subsurface ocean dynamics?, *Icarus*, *310*, 149–164, doi:10.1016/j.icarus.2017.12.010.
- Lambeck, K., H. Rouby, A. Purcell, Y. Sun, and M. Sambridge (2014), Sea level and global ice volumes from the Last Glacial Maximum to the Holocene, *Proc. Nat. Acad. Sci.*, *111*(43), 15,296–15,303, doi:10.1073/pnas.1411762111.
- Lambert, W. D. (1930), The form of the geoid on the hypothesis of complete isostatic compensation, *Bull. G eod.*, *26*, 98–106, doi:0.1007/BF03030028.
- Lau, H. C. P., J. X. Mitrovica, J. Austermann, O. Crawford, D. Al-Attar, and K. Latychev (2016), Inferences of mantle viscosity based on ice age data sets: Radial structure, *J. Geophys. Res.*, *121*(10), 6991–7012, doi:10.1002/2016JB013043.
- McGovern, P. J., S. C. Solomon, D. E. Smith, M. T. Zuber, M. Simons, M. A. Wieczorek, R. J. Phillips, G. A. Neumann, O. Aharonson, and J. W. Head (2002), Localized gravity/topography admittance and correlation spectra on Mars: Implications for regional and global evolution, *J. Geophys. Res.*, *107*, 5136, doi:10.1029/2002JE001854.
- McGovern, P. J., S. C. Solomon, D. E. Smith, M. T. Zuber, M. Simons, M. A. Wieczorek, R. J. Phillips, G. A. Neumann, O. Aharonson, and J. W. Head (2004), Correction to “Localized gravity/topography admittance and correlation spectra on Mars: Implications for regional and global evolution”, *J. Geophys. Res.*, *109*, E07007, doi:10.1029/2004JE002286.
- McKenzie, D., F. Nimmo, J. A. Jackson, P. B. Gans, and E. L. Miller (2000), Characteristics and consequences of flow in the lower crust, *J. Geophys. Res.*, *105*(B5), 11,029–11,046, doi:10.1029/1999JB900446.
- McKinnon, W. B. (2015), Effect of Enceladus’s rapid synchronous spin on interpretation of Cassini gravity, *Geophys. Res. Lett.*, *42*, 2137–2143, doi:10.1002/2015GL063384.

- Melosh, H. J. (2011), *Planetary Surface Processes*, Cambridge University Press, Cambridge.
- Meyer, J., and J. Wisdom (2008), Episodic volcanism on Enceladus: Application of the Ojakangas Stevenson model, *Icarus*, *198*(1), 178–180, doi:10.1016/j.icarus.2008.06.012.
- Mitrovića, J. X. (1996), Haskell [1935] revisited, *J. Geophys. Res.*, *101*(B1), 555–569, doi:10.1029/95JB03208.
- Mitrovića, J. X., and J. Wahr (2011), Ice age Earth rotation, *Ann. Rev. Earth Planet. Sci.*, *39*, 577–616, doi:10.1146/annurev-earth-040610-133404.
- Mohit, P. S., and R. J. Phillips (2006), Viscoelastic evolution of lunar multiring basins, *J. Geophys. Res.*, *111*(E12), E12001, doi:10.1029/2005JE002654.
- Mohit, P. S., and R. J. Phillips (2007), Viscous relaxation on early Mars: A study of ancient impact basins, *Geophys. Res. Lett.*, *34*(21), L21204, doi:10.1029/2007GL031252.
- Mohit, P. S., C. L. Johnson, O. Barnouin-Jha, M. T. Zuber, and S. C. Solomon (2009), Shallow basins on Mercury: Evidence of relaxation?, *Earth Planet. Sci. Lett.*, *285*(3-4), 355–363, doi:10.1016/j.epsl.2009.04.023.
- Nimmo, F., and B. G. Bills (2010), Shell thickness variations and the long-wavelength topography of Titan, *Icarus*, *208*, 896–904, doi:10.1016/j.icarus.2010.02.020.
- Nimmo, F., A. C. Barr, M. Běhouňková, and W. B. McKinnon (2018), The thermal and orbital evolution of Enceladus: observational constraints and models, in *Enceladus and the Icy Moons of Saturn*, edited by P. M. Schenk, R. N. Clark, C. J. A. Howett, A. J. Verbiscer, and J. Hunter Waite, pp. 79–94, University of Arizona Press, Tucson, doi:10.2458/azu_uapress_9780816537075-ch005.
- Ojakangas, G. W., and D. J. Stevenson (1986), Episodic volcanism of tidally heated satellites with application to Io, *Icarus*, *66*(2), 341–358, doi:10.1016/0019-1035(86)90163-6.
- Park, R. S., A. S. Konopliv, A. I. Ermakov, J. C. Castillo-Rogez, R. R. Fu, K. H. G. Hughson, T. H. Prettyman, C. A. Raymond, J. E. C. Scully, H. G. Sizemore, M. M. Sori, A. T. Vaughan, G. Mitri, B. E. Schmidt, and C. T. Russell (2020), Evidence of non-uniform crust of Ceres from Dawn’s high-resolution gravity data, *Nat. Astr.*, *4*, 748–755, doi:10.1038/s41550-020-1019-1.
- Parmentier, E. M., and J. W. Head (1981), Viscous relaxation of impact craters on icy planetary surfaces: Determination of viscosity variation with depth, *Icarus*, *47*(1), 100–111, doi:10.1016/0019-1035(81)90095-6.
- Passey, Q. R. (1983), Viscosity of the lithosphere of Enceladus, *Icarus*, *53*(1), 105–120, doi:10.1016/0019-1035(83)90024-6.
- Pathare, A. V., D. A. Paige, and E. Turtle (2005), Viscous relaxation of craters within the martian south polar layered deposits, *Icarus*, *174*(2), 396–418, doi:10.1016/j.icarus.2004.10.031.
- Pauer, M., K. Fleming, and O. Čadek (2006), Modeling the dynamic component of the geoid and topography of Venus, *J. Geophys. Res.*, *111*(E11), E11012, doi:10.1029/2005JE002511.
- Peltier, R. (1982), Dynamics of the Ice Age Earth, *Adv. Geophys.*, *24*, 1–146, doi:10.1016/S0065-2687(08)60519-1.
- Peltier, W. R. (1974), The impulse response of a Maxwell Earth., *Rev. Geophys. Space Phys.*, *12*, 649–669, doi:10.1029/RG012i004p00649.
- Peltier, W. R. (1976), Glacial-isostatic adjustment - II. The inverse problem, *Geophys. J. R. astr. Soc.*, *46*(3), 669–705, doi:10.1111/j.1365-246X.1976.tb01253.x.
- Peltier, W. R. (1985), The LAGEOS constraint on deep mantle viscosity: Results from a new normal mode method for the inversion of viscoelastic relaxation spectra, *J. Geophys. Res.*, *90*(B11), 9411–9422, doi:10.1029/JB090iB11p09411.
- Peltier, W. R. (2004), Global Glacial Isostasy and the Surface of the Ice-Age Earth: The ICE-5G (VM2) Model and GRACE, *Ann. Rev. Earth Planet. Sci.*, *32*, 111–149, doi:10.1146/annurev.earth.32.082503.144359.

- Peltier, W. R., D. F. Argus, and R. Drummond (2015), Space geodesy constrains ice age terminal deglaciation: The global ICE-6G_C (VM5a) model, *J. Geophys. Res.*, *120*(1), 450–487, doi:10.1002/2014JB011176.
- Phillips, R. J., and K. Lambeck (1980), Gravity fields of the terrestrial planets: long-wavelength anomalies and tectonics., *Reviews of Geophysics and Space Physics*, *18*, 27–76, doi:10.1029/RG018i001p00027.
- Qin, C., S. Zhong, and R. Phillips (2018), Formation of the lunar fossil bulges and its implication for the early Earth and Moon, *Geophys. Res. Lett.*, *45*(3), 1286–1296, doi:10.1002/2017GL076278.
- Ramberg, H. (1968), Fluid dynamics of layered systems in the field of gravity, a theoretical basis for certain global structures and isostatic adjustment, *Phys. Earth Planet. Int.*, *1*(2), 63–87, doi:10.1016/0031-9201(68)90051-4.
- Ribe, N. M. (2015), Analytical approaches to mantle dynamics, in *Treatise on Geophysics*, edited by G. Schubert, second ed., pp. 145–196, Elsevier, Oxford, doi:10.1016/B978-0-444-53802-4.00129-9.
- Ribe, N. M. (2018), *Theoretical Mantle Dynamics*, Cambridge University Press, doi:10.1017/9781316795897.
- Ricard, Y., L. Fleitout, and C. Froidevaux (1984), Geoid heights and lithospheric stresses for a dynamic Earth, *Annales Geophysicae*, *2*, 267–285.
- Richards, M. A., and B. H. Hager (1984), Geoid anomalies in a dynamic earth, *J. Geophys. Res.*, *89*(B7), 5987–6002, doi:10.1029/JB089iB07p05987.
- Robuchon, G., F. Nimmo, J. Roberts, and M. Kirchoff (2011), Impact basin relaxation at Iapetus, *Icarus*, *214*(1), 82–90, doi:10.1016/j.icarus.2011.05.011.
- Sabadini, R., B. Vermeersen, and G. Cambiotti (2016), *Global Dynamics of the Earth, 2nd Ed.*, Springer, Dordrecht, doi:10.1007/978-94-017-7552-6.
- Segatz, M., T. Spohn, M. N. Ross, and G. Schubert (1988), Tidal dissipation, surface heat flow, and figure of viscoelastic models of Io, *Icarus*, *75*, 187–206, doi:10.1016/0019-1035(88)90001-2.
- Simons, M., S. C. Solomon, and B. H. Hager (1997), Localization of gravity and topography: Constraints on the tectonics and mantle dynamics of Venus, *Geophys. J. Int.*, *131*, 24–31, doi:10.1111/j.1365-246X.1997.tb00593.x.
- Smrekar, S. E., and R. J. Phillips (1991), Venusian highlands: geoid to topography ratios and their implications, *Earth Planet. Sci. Lett.*, *107*(3-4), 582–597, doi:10.1016/0012-821X(91)90103-O.
- Solomon, S. C., R. P. Comer, and J. W. Head (1982), The evolution of impact basins: viscous relaxation of topographic relief., *J. Geophys. Res.*, *87*, 3975–3992, doi:10.1029/JB087iB05p03975.
- Sori, M. M., S. Byrne, M. T. Bland, A. M. Bramson, A. I. Ermakov, C. W. Hamilton, K. A. Otto, O. Ruesch, and C. T. Russell (2017), The vanishing cryovolcanoes of Ceres, *Geophys. Res. Lett.*, *44*(3), 1243–1250, doi:10.1002/2016GL072319.
- Sori, M. M., P. B. James, B. C. Johnson, J. M. Soderblom, S. C. Solomon, M. A. Wieczorek, and M. T. Zuber (2018), Isostatic compensation of the lunar highlands, *J. Geophys. Res.*, *123*(2), 646–665, doi:10.1002/2017JE005362.
- Spada, G., V. R. Barletta, V. Klemann, R. E. M. Riva, Z. Martinec, P. Gasperini, B. Lund, D. Wolf, L. L. A. Vermeersen, and M. A. King (2011), A benchmark study for glacial isostatic adjustment codes, *Geophys. J. Int.*, *185*, 106–132, doi:10.1111/j.1365-246X.2011.04952.x.
- Steffen, H., and P. Wu (2011), Glacial isostatic adjustment in Fennoscandia—A review of data and modeling, *J. Geodyn.*, *52*(3), 169–204, doi:10.1016/j.jog.2011.03.002.
- Thomas, P. J., and S. W. Squyres (1988), Relaxation of impact basins on icy satellites, *J. Geophys. Res.*, *93*, 14,919–14,932, doi:10.1029/JB093iB12p14919.
- Turcotte, D. L., and G. Schubert (2014), *Geodynamics - 3rd Edition*, 626 pp., Cambridge University Press, Cambridge, doi:10.1017/CBO9780511843877.
- Vening Meinesz, F. A. (1946), The indirect isostatic or Bowie reduction and the equilibrium figure of the Earth, *Bull. Géod.*, *1*, 33–107, doi:10.1007/BF02519025.

- Wang, R. (1997), Tidal response of the solid earth, in *Tidal phenomena, Lecture notes in Earth sciences*, vol. 66, edited by H. Wilhelm, W. Zürn, and H.-G. Wenzel, pp. 27–57, Springer Berlin Heidelberg, doi:10.1007/BFb0011456.
- White, O. L., P. M. Schenk, and A. J. Dombard (2013), Impact basin relaxation on Rhea and Iapetus and relation to past heat flow, *Icarus*, *223*(2), 699–709, doi:10.1016/j.icarus.2013.01.013.
- White, O. L., P. M. Schenk, A. W. Bellagamba, A. M. Grimm, A. J. Dombard, and V. J. Bray (2017), Impact crater relaxation on Dione and Tethys and relation to past heat flow, *Icarus*, *288*, 37–52, doi:10.1016/j.icarus.2017.01.025.
- Whitehouse, P. L. (2018), Glacial isostatic adjustment modelling: historical perspectives, recent advances, and future directions, *Earth Surf. Dynam.*, *6*(2), 401–429, doi:10.5194/esurf-6-401-2018.
- Wu, P., and W. R. Peltier (1982), Viscous gravitational relaxation, *Geophys. J. R. astr. Soc.*, *70*(2), 435–485, doi:10.1111/j.1365-246X.1982.tb04976.x.
- Zannoni, M., D. Hemingway, L. Gomez Casajus, and P. Tortora (2020), The gravity field and interior structure of Dione, *Icarus*, *345*, 113713, doi:10.1016/j.icarus.2020.113713.
- Zhong, S. (1997), Dynamics of crustal compensation and its influences on crustal isostasy, *J. Geophys. Res.*, *102*(B7), 15,287–15,299, doi:10.1029/97JB00956.
- Zhong, S. (2002), Effects of lithosphere on the long-wavelength gravity anomalies and their implications for the formation of the Tharsis rise on Mars, *J. Geophys. Res.*, *107*(E7), 5054, doi:10.1029/2001JE001589.
- Zhong, S., and M. T. Zuber (2000), Long-wavelength topographic relaxation for self-gravitating planets and implications for the time-dependent compensation of surface topography, *J. Geophys. Res.*, *105*, 4153–4164, doi:10.1029/1999JE001075.